

Observations of Bedform Migration and Bedload Sediment Transport in Combined Wave-Current Flows

Wengrove, M. E.; Foster, D. L.; Lippmann, T. C.; de Schipper, M. A.; Calantoni, J.

DOI

[10.1029/2018JC014555](https://doi.org/10.1029/2018JC014555)

Publication date

2019

Document Version

Accepted author manuscript

Published in

Journal of Geophysical Research: Oceans

Citation (APA)

Wengrove, M. E., Foster, D. L., Lippmann, T. C., de Schipper, M. A., & Calantoni, J. (2019). Observations of Bedform Migration and Bedload Sediment Transport in Combined Wave-Current Flows. *Journal of Geophysical Research: Oceans*, 124(7), 4572-4590. <https://doi.org/10.1029/2018JC014555>

Important note

To cite this publication, please use the final published version (if applicable). Please check the document version above.

Copyright

Other than for strictly personal use, it is not permitted to download, forward or distribute the text or part of it, without the consent of the author(s) and/or copyright holder(s), unless the work is under an open content license such as Creative Commons.

Takedown policy

Please contact us and provide details if you believe this document breaches copyrights. We will remove access to the work immediately and investigate your claim.

Observations of Time Dependent Bedform Transformation in Combined Wave-Current Flows

M. E. Wengrove¹, D. L. Foster¹, T. C. Lippmann², M. A. de Schipper³, J. Calantoni⁴

¹University of New Hampshire, Ocean Engineering

²University of New Hampshire, Earth Sciences

³Delft University of Technology, Hydraulic Engineering

⁴Marine Geosciences Division, U.S. Naval Research Laboratory

¹24 Colovos Road Durham, NH 03824

Key Points:

- Bedform building is a time dependent process, especially important in combined wave current flows.
- The sediment continuity equation or Exner equation can be used to estimate bedform volume change.
- Contribution of unique dataset of combined waves and current influence on bottom roughness.

Abstract

Although combined wave-current flows in the nearshore coastal zone are common, there are few observations of bedform response and inherent geometric scaling in combined flows. Our effort presents observations of bedform dynamics that were strongly influenced by waves, currents, and combined wave-current flow at two sampling locations separated by 60 m in the cross shore. Observations were collected in 2014 at the Sand Engine mega-nourishment on the Delfland coast of The Netherlands. The bedforms had wavelengths ranging from 14 cm to over 2 m and transformed shape and orientation within, at times, as little as 20 minutes and up to 6 hours. The dynamic set of observations was used to evaluate a fully unsteady description of changes in the bedform growth with the sediment transport continuity equation (Exner equation), relating changes in bedform volume to bedload sediment transport. Analysis shows that bedform volume was a function of the integrated transport rate over the bedform development time period. The bedform development time period (time lag of bedform growth/adjustment) is important for estimating changes in bedform volume. Results show that this continuity principle held for wave, current, and combined wave-current generated bedforms.

1 Introduction

Time varying wave, current, and combined wave-current flows are characteristic of most nearshore regions (e.g. *Grant and Madsen [1979]; Passchier and Kleinans [2005]; Soulsby and Clarke [2005]*). These complex hydrodynamic environments are complicated with small scale bed roughness (e.g. sand ripples and megaripples) that have a two way feedback with the local hydrodynamics, apparent within nearshore modeling [*Wikramanayake and Madsen, 1994; Lesser et al., 2004; Ganju and Sherwood, 2010*]. Previous research demonstrates that characteristic bedform roughness lengths (bedform wavelength and height) scale with the hydrodynamic forcing applied to the seabed under waves or currents (e.g. *Fredsøe [1984]; Clifton and Dingler [1984]; Wiberg and Harris [1994]; Traykovski et al. [1999]; Hay and Mudge [2005]*). However, there have been very few studies of bedform scaling and orientation in response to dynamically changing forcing that includes combined wave-current flows [*Li and Amos, 1998; Hay and Mudge, 2005; Lacy et al., 2007; Soulsby et al., 2012; Nelson and Voulgaris, 2015*].

For combined wave-current flows, most of the literature addresses the transition of bedforms between flow states with observations of relatively small bedforms with wave-

48 lengths of less than 0.5 m under relatively low energy wave conditions or with waves plus
49 weak mean flow (e.g. *Grant and Madsen* [1979]; *Li and Amos* [1998]; *Soulsby and Clarke*
50 [2005]; *Lacy et al.* [2007]; *Soulsby et al.* [2012]). Results of these efforts show that com-
51 bined flow bedforms are less steep than wave dominant bedforms, and generally orient in
52 a pattern influenced by the maximum gross bedform normal transport direction [*Gallagher*
53 *et al.*, 1998; *Lacy et al.*, 2007]. There are a limited number efforts that observe larger scale
54 bedforms, like megaripples, in wave dominant or combined flows (*Gallagher et al.* [1998];
55 *Gallagher* [2003]; *Larsen et al.* [2015]), but these efforts do not address characteristics of
56 bedform response to transition periods.

57 Observations of bedforms under wave dominant or current dominant flows suggests
58 that bedform building is a time dependent process (e.g. *Davis et al.* [2004]; *Testik et al.*
59 [2005]; *Doucette and O'Donoghue* [2006]; *Austin et al.* [2007]; *Traykovski* [2007]; *Soulsby*
60 *et al.* [2012]; *Nelson and Voulgaris* [2015]). The bedform shape and volume is depen-
61 dent on present hydrodynamic conditions, as well as past forcing. Time-dependent bed-
62 form models that estimate roughness length scales use a departure from equilibrium ap-
63 proach (e.g. *Traykovski* [2007]; *Soulsby et al.* [2012]) that assumes bedform length scales
64 are being driven toward equilibrium with the present hydrodynamic conditions. The as-
65 sumption is generally valid for waves [*Davis et al.*, 2004; *Testik et al.*, 2005; *Doucette and*
66 *O'Donoghue*, 2006; *Traykovski*, 2007]; however, present equilibrium theory may not cap-
67 ture the physics of bedform adjustment in combined wave-current flows because the time
68 constants associated with current models may not be appropriate to represent dynamics in
69 combined flows [*Austin et al.*, 2007].

70 In our effort, we present observations of ripple and megaripple formation in re-
71 sponse to high energy combined flows with, at times, the addition of a strong current.
72 Forcing conditions ranged from wave dominant flow, to combined wave-current flow, to
73 mean current flow. Bedform transition periods and growth cycles were observed in re-
74 sponse to the variable flow conditions. Additionally, the results demonstrate that the sed-
75 iment continuity equation, or Exner equation, captures bedform building as a time depen-
76 dent process, suggesting that the sediment continuity equation may be used to model dy-
77 namic roughness in the nearshore, especially relevant when considering combined wave-
78 current flows.

79 2 Methods

80 2.1 Experiment and Instrumentation

81 Data were collected during a field campaign at the Sand Engine mega-nourishment
 82 as a part of the MEGA-Perturbation EXperiment (MEGAPEX) in the fall of 2014 on the
 83 Delfland Coast of the Netherlands [*Radermacher et al.*, 2017]. Since the installment of
 84 the 21.5 million cubic meters of sand in 2011, the Sand Engine has dramatically changed
 85 shape [*Stive et al.*, 2013]; in 2011 it stretched 2 km in the alongshore and 1 km into the
 86 North Sea, and in 2014 it stretched 4 km alongshore and 800 m in the cross shore [*Ra-*
 87 *dermacher et al.*, 2017]. The large scale morphology is considered very dynamic with ob-
 88 servable bathymetric changes over periods of days to months. Our effort investigates the
 89 dynamic nature of the small scale morphology at the seaward tip of the Sand Engine.

90 Local small scale morphology and hydrodynamics were observed between the shore-
 91 line and the shore-parallel sandbar that were 136 m apart at two cross shore stations, S1
 92 and S2, at the tip of the Sand Engine (Figure 1a). S1 was located 20 m seaward of the
 93 low tide shoreline and S2 was located 66 m further offshore and 50 m shoreward of the
 94 subtidal sandbar. Morphology was sampled at each location with a stationary sweeping
 95 and rotating 1 MHz Imagenex 881a pencil beam sonar with a 3 m diameter footprint. S1
 96 was sampled every 20 minutes with a 1.4° sweep step and a 2.4° rotation step from 26
 97 Sept. to 23 Oct. 2014 (day of year 269-296), and S2 was sampled every 2 hours with
 98 a 1.4° sweep step and a 1.4° rotation step from 2 Oct. to 18 Oct. (day of year 275 to
 99 291). Hydrodynamic forcing was measured at S1 using a downward looking high reso-
 100 lution acoustic Doppler current profiler (ADCP) positioned 0.4 m above the seabed and
 101 burst sampled for 20 minutes every hour at 4 Hz, and at S2 using an acoustic Doppler
 102 velocimeter (ADV) positioned 1 m above the seabed and burst sampled for 20 minutes
 103 every hour at 64 Hz (Figure 1b). The mean lower low water depth at S1 was -1.0 m NAP
 104 (Normaal Amsterdam Peil, approximately mean sea level) and at S2 was -1.7 m NAP and
 105 the median sediment grain size of the quartz sediment at both sites was 350 μm . The
 106 tidal range was approximately 1.5 m. Large scale bathymetry was measured with an echo
 107 sounder during regular jet ski surveys. The large scale coordinate system used through-
 108 out this paper is with respect to degrees from shore-normal, with 0° being onshore (-x),
 109 +90° rotating counterclockwise from shore normal, and -90° rotating clockwise from shore
 110 normal.

2.2 Hydrodynamics

The local flow at each monitoring station was decomposed into current velocities, with magnitude U and direction ϕ_c , and wave orbital velocities, with magnitude u_o and direction ϕ_w , over 10 minute averaged time intervals. The current velocity is defined by the resultant of the temporal mean of the horizontal (u , v) velocities with ,

$$U = |\bar{u}|, \quad (1)$$

and the overbar represents a temporal average over 10 minutes. The magnitude of the orbital velocity assumes a sinusoidal velocity with,

$$u_o = \sqrt{2}u_{std}, \quad (2)$$

where $u_{std} = \overline{[(u - U)^2]^{0.5}}$ [Traykovski *et al.*, 1999]. The wave period is defined with,

$$T = \frac{2\pi}{S_{m_2}/S_{m_1}}, \quad (3)$$

where S is the spectra of the pressure signal, and the subscripts m_1 and m_2 refer to the first (mean) and second (variance) moments of the spectra [Madsen *et al.*, 1988]. The wave orbital diameter was defined with

$$d_o = 2\frac{u_o}{2\pi/T}. \quad (4)$$

The combined wave current velocity [Lacy *et al.*, 2007] relates the wave orbital and current velocities with a third term representing the combined effect depending on the angle between the orbital and current velocities, where

$$u_{wc} = [u_o^2 + U^2 + 2u_oU \cos |\phi_w - \phi_c|]^{0.5}. \quad (5)$$

Finally, the maximum kinetic energy in the combined wave-current flows is defined as

$$E_{k_{wc}} = \frac{1}{2}u_{wc}^2. \quad (6)$$

In our observations we distinguish between wave dominant, current dominant and combined flow conditions using a fraction-of-energy approach to assess the contribution of waves and/or currents to sediment flux. $E_{k_{wc}}$ is defined as the maximum kinetic energy in the flow field including both waves and currents. $E_{k_w}/E_{k_{wc}}$ is defined as the fraction of kinetic energy due to waves. A value of 1 would be purely wave driven flow, and

132 a value of 0 would be purely current driven flow. Previous literature has distinguished
 133 wave dominant flows from combined flows based on a ratio of wave induced to current
 134 induced friction velocity, where purely wave ripples occur at a friction velocity ratio of
 135 0.5 or greater [*Li and Amos, 1998; Lacy et al., 2007*]. The estimate of friction velocity can
 136 vary based upon the method used to estimate the bed shear stress, where $u_* = (\tau_b/\rho)^{1/2}$.
 137 Due to the wide variability in friction velocity estimates, friction velocity was not used
 138 to evaluate the relative strength of the waves and currents. The ratio of wave and cur-
 139 rent dominant flow is highly dependent upon the method(s) chosen for the estimates of
 140 the wave and current friction velocity. Rather, we choose to express the relative strength
 141 of waves and currents as a function of the total kinetic energy. To put this limit from
 142 [*Lacy et al., 2007*] in terms of energy, the threshold of 0.5 is squared. Therefore we de-
 143 fine, $E_{k_w}/E_{k_{wc}} > 0.75$ to be wave dominant, $0.75 \geq E_{k_w}/E_{k_{wc}} \geq 0.25$ for combined wave-
 144 current flow, and $0.25 > E_{k_w}/E_{k_{wc}}$ to be current dominant. An energy approach is used
 145 instead of the friction velocity due to the high uncertainties associated with estimating
 146 the friction velocity in combined flow conditions (particularly when the bedform field is
 147 highly dynamic). The kinetic energy was either measured or calculated using linear wave
 148 theory for the wave contribution and a log layer approximation for the mean flow contri-
 149 bution. Calculated values were attenuated through the water column to approximately 10
 150 cm above the crest of the bedforms.

151 **2.3 Measured Bedform Statistics**

152 Statistics of bedform wavelength (λ), bedform height (η), and bedform orientation
 153 (ϕ_r) are determined through analysis of sonar return data. Bottom position within each
 154 sonar dataset was found by identifying the high intensity return region for each sonar ping
 155 using two methods. The first is a weighted mean sum (WMS) method and the second is
 156 a bearing direction indicator (BDI) method [*SeaBeam, 2000*]. WMS applies a weighted
 157 mean sum to each sonar ping, where the location of the highest WMS for each beam is
 158 the location of the bed. The WMS method works well for return data with high grazing
 159 angles (data within 30° of the sonar nadir). The BDI applies a parabolic fit to the high
 160 intensity return for all the beams intersecting the same section of bed within one sweep
 161 over multiple pings. The BDI method is suited to intensity returns at low grazing angles
 162 since the multiple ping fit gives higher confidence in bed location. WMS was used to de-
 163 tect the bed within the inner 1 m diameter at bed level and BDI was used to detect the

164 bed from the 1 m diameter range to the sonar sampling extent at bed level (see *Wengrove*
 165 *et al.* [2017] for more detail).

166 With a time series of 2D local bathymetries (Figures 2f-h and 3f-h), the dominant
 167 ripple wavelengths, heights, and orientations were determined with normalized 2D spatial
 168 wavenumber spectral analysis [*Maier and Hay, 2009; Becker et al., 2007*]. The 2D spatial
 169 spectra, S (m^3), have axes of wavenumber, k_x (cross shore) and k_y (alongshore) ($1/\text{m}$).
 170 The spectra were normalized by premultiplying S by the wavenumber k_x and k_y , where
 171 $\hat{S} = Sk_xk_y$ [*Alamo and Jimenez, 2003*]. The benefit of a normalized spectra is that the
 172 multiplication by wavenumber emphasizes higher wavenumbers and enhances the energy
 173 peaks of interest for analysis. The energy distribution in the spectra indicate the domi-
 174 nant bedform wave number and orientation. The bedform wavelength is defined as the
 175 bedform-normal distance from crest to crest, and the bedform height is defined as the ver-
 176 tical distance between bedform trough and crest. Estimates of bedform height are found by
 177 integrating the spectrum, analogous to a significant ocean wave height calculation from
 178 temporal spectral analysis [*Traykovski, 2007; Penko et al., 2017*] (see [*Wengrove et al.,*
 179 *2017*] for more detail).

180 The uncertainties associated with the spatial resolution of the pencil beam sonar
 181 measurements were related to range resolution, beam width, and sweep and rotation step
 182 angles. During the course of the experiment the water temperature stayed relatively con-
 183 stant with time, and a sound speed of 1502 m/s was used to convert sonar time returns
 184 into range estimates. The range resolution of the pencil beam is 2 mm for a sampling
 185 range of 1 m to 4 m. The conical beam width operating at 1 MHz is 1.4° , so 1 m away
 186 from the transducer (within 30° of the sonar nadir) the resolution limit is 2.5 cm, while
 187 at the profiling extent or approximately 2 m way from the transducer, the resolution limit
 188 becomes 5.0 cm. Finally, with respect to spatial sampling step angle, for S1, directly un-
 189 der the sonar the spatial resolution was 2 cm x 4 cm and at the radial edge of the swath
 190 the spatial resolution was 5 cm x 8 cm. For S2, directly under the sonar the spatial res-
 191 olution was 2 cm x 2 cm and at the profiling extent the spatial resolution was 5 cm x 5
 192 cm. With these limitations, the smallest bedform wavelength that could be resolved within
 193 the inner 30° of the sonar nadir was approximately 12 cm, and at the profiling extent was
 194 approximately 25 cm. Bedform height could be resolved within 2 cm.

195 Uncertainties associated with the temporal resolution of the bedform migration in-
 196 volve the timescale for the sonar sensor rotations. Bedload sediment transport processes
 197 with a time scale less than a full sweep-rotation time window were not resolved; for S1
 198 this was 10 minutes and for S2 this was 15 minutes. Additionally, processes that occurred
 199 with a time scale of less than the time between subsequent sonar scans, dt , were not re-
 200 solved; dt was 20 minutes for S1 and 2 hours for S2. However, the low noise floor of the
 201 spectra of the time series of observed bedform wavelengths over the month long deploy-
 202 ment at S1 showed that there were no sign of aliasing with a dt of 20 minutes for estimat-
 203 ing migration rates (not shown), so a dt of 15 minutes to estimate migration rates at S2 is
 204 considered sufficient as well.

205 2.4 Sediment Continuity Equation

206 Assuming a sinusoidal function for transport,

$$\mathbf{q}_b = q_b \cos \left[\frac{2\pi}{\lambda} \left(V_{mig} \cdot t - x_b - \delta_{x_b} \right) \right], \quad (7)$$

207 where \mathbf{q}_b is the bedload sediment flux [$\text{m}^3/\text{m}/\text{s}$], q_b is the scalar transport, V_{mig} is the
 208 migration rate, t is time, λ is the wave length, δ_{x_b} is the phase offset between the bedform
 209 shape and the function for transport, x_b is the position along the bedform wavelength, and
 210 t is time. Using $\cos(\alpha - \beta) = \cos(\alpha)\cos(\beta) + \sin(\alpha)\sin(\beta)$,

$$q_b = q_1 \cos \left[\frac{2\pi}{\lambda} \left(V_{mig} \cdot t - x_b \right) \right] + q_2 \sin \left[\frac{2\pi}{\lambda} \left(V_{mig} \cdot t - x_b \right) \right], \quad (8)$$

$$q_1 = q_b \cos \left(\frac{2\pi}{\lambda} \delta_{x_b} \right), q_2 = q_b \sin \left(\frac{2\pi}{\lambda} \delta_{x_b} \right), \quad (9)$$

212 and $q_2/q_1 = \tan(\frac{2\pi}{\lambda} \delta_{x_b})$.

213 We assume the bed level, z_b , as

$$z_b(x, t) = \eta \cos \left[\frac{2\pi}{\lambda} \left(V_{mig} \cdot t - x_b \right) \right]. \quad (10)$$

214 where η is the amplitude of the bedform. The bedform height, wavelength, and migration
 215 rate are allowed to be fully unsteady.

216 The sediment continuity equation, or the Exner equation, relates the sediment flux
 217 gradient per unit width to the rate of bed level change [*Nielsen, 1992*], and is commonly

218 expressed with

$$\frac{\partial q_b}{\partial x} \equiv -n \frac{\partial z_b}{\partial t}. \quad (11)$$

219 where n is the sediment packing (~ 0.7 for sand). For the case of bedform migration or
 220 transformation with no local accretion or erosion, the bed elevation, z_b , can be expressed
 221 by the local bedform geometry ($z_b = \eta$). By taking the spatial derivative of the expression
 222 for q_b and the temporal derivative of the expression for z_b , and assuming that η , λ , and
 223 $V_{mig.}$ are a function of t , but q_1 and q_2 are not a function of x , then,

$$\frac{\partial q_b}{\partial x} = q_1 \frac{2\pi}{\lambda} \sin \left[\frac{2\pi}{\lambda} (V_{mig.} t - x_b) \right] - q_2 \frac{2\pi}{\lambda} \cos \left[\frac{2\pi}{\lambda} (V_{mig.} t - x_b) \right] \quad (12)$$

224 and

$$\frac{\partial z_b}{\partial t} = \frac{\partial \eta}{\partial t} \cos \left[\frac{2\pi}{\lambda} (V_{mig.} t - x) \right] - \eta \left[2\pi \left(\frac{t}{\lambda} \frac{\partial V_{mig.}}{\partial t} + V_{mig.} t \frac{\partial}{\partial t} \frac{1}{\lambda} + \frac{V_{mig.}}{\lambda} - x_b \frac{\partial}{\partial t} \frac{1}{\lambda} \right) \right] \sin \left[\frac{2\pi}{\lambda} (V_{mig.} t - x) \right]. \quad (13)$$

225 Now, using (12) and (13) in (11) and the definition if $ax + by = mx + ny$ then $a = m$ and
 226 $b = n$, shows that

$$n\eta \left[2\pi \left(\frac{t}{\lambda} \frac{\partial V_{mig.}}{\partial t} + V_{mig.} t \frac{\partial}{\partial t} \frac{1}{\lambda} + \frac{V_{mig.}}{\lambda} - x_b \frac{\partial}{\partial t} \frac{1}{\lambda} \right) \right] = \frac{2\pi}{\lambda} q_1, \quad (14)$$

227 and

$$n \frac{\partial \eta}{\partial t} = \frac{2\pi}{\lambda} q_2 \quad (15)$$

228 where (14) represents the unsteady sediment flux from the migrating bedform, and (15)
 229 represents the unsteady sediment flux from a growing or decaying bedform. Expressions
 230 for the bedform migration and growth with a semi-steady assumption for the bedform λ
 231 and $V_{mig.}$ can be found in *Nielsen* [1992] and *Roelvink and Reniers* [2011]. Both (14) and
 232 (15) are theoretically equivalent, by substituting (9) into (14) and (15), and equating the
 233 result by means of q_b gives,

$$\frac{\partial \eta}{\partial t} = 2\pi\eta \left(\frac{t}{\lambda} \frac{\partial V_{mig.}}{\partial t} + V_{mig.} t \frac{\partial}{\partial t} \frac{1}{\lambda} + \frac{V_{mig.}}{\lambda} - x_b \frac{\partial}{\partial t} \frac{1}{\lambda} \right) \tan \left(\frac{2\pi}{\lambda} \delta_{x_b} \right). \quad (16)$$

234 An expression for δ_{x_b}/λ as a function of $\partial\eta/\partial t$ and $V_{mig.}$ follows,

$$\delta_{x_b}/\lambda = \frac{1}{2\pi} \tan^{-1} \left[\frac{\partial\eta}{\partial t} / \left(2\pi\eta \left(\frac{t}{\lambda} \frac{\partial V_{mig.}}{\partial t} + V_{mig.} t \frac{\partial}{\partial t} \frac{1}{\lambda} + \frac{V_{mig.}}{\lambda} - x_b \frac{\partial}{\partial t} \frac{1}{\lambda} \right) \right) \right]. \quad (17)$$

235 The bedform volumetric change as a function of the sediment flux is found begin-
 236 ning with (15) and expanding the time rate of change in bedform height with the product
 237 rule,

$$\frac{n\lambda}{2\pi} \frac{\partial\eta}{\partial t} = \frac{n}{2\pi} \frac{\partial\eta\lambda}{\partial t} - \frac{n}{2\pi} \frac{\eta\partial\lambda}{\partial t}. \quad (18)$$

238 By substituting the expression for q_2 and integrating the manipulation from $t - \tau$ to t , an
 239 expression for the bedform volumetric change is given as

$$\Delta\Lambda_b = \Delta \frac{n}{2} \eta \lambda = \int_{t-\tau}^t \pi q_b \sin(2\pi\delta_{x_b}/\lambda) dt + \int_{t-\tau}^t \frac{n}{2} \frac{\eta\partial\lambda}{\partial t} dt. \quad (19)$$

240 where $\Delta \frac{n}{2} \eta \lambda$ is the change in volume of the bedform, $\Delta\Lambda_b$, over some time since it started
 241 to grow or decay, $\tau - t$, to the present time, t . The first term on the right hand side is the
 242 portion of the time integrated sediment flux related to bedform growth or decay. The sec-
 243 ond term on the right hand side of (19) is related to the bedform stretching over time. The
 244 expression represents a fully unsteady derivation of bedform transformation and translation
 245 with respect to bedform height, wavelength, and migration.

246 **2.5 Existing Time-Dependent Bedform Geometry Models**

247 In laboratory settings *Davis et al.* [2004], *Smith and Sleath* [2005], *Testik et al.* [2005],
 248 and *Doucette and O'Donoghue* [2006] explored the time dependent nature of bedforms be-
 249 tween equilibrium conditions, as well as the associated time scale for bedforms to reach an
 250 asymptotic equilibrium state with imposed wave forcing conditions. These studies give es-
 251 timates for bedform temporal adjustment to equilibrium based on sediment transport rates,
 252 with each showing that it takes time for bedforms to evolve and grow between equilibrium
 253 states. In field settings, *Traykovski* [2007], *Soulsby et al.* [2012], and *Nelson and Voulgaris*
 254 [2015] also take a departure from equilibrium approach by relating a change in geometry
 255 over a period of time to a departure from equilibrium geometry model that imposes a pa-
 256 rameterized time scale of change. Our effort further considers the wave-only spectral time

257 dependent model of *Traykovski* [2007], and the wave or current dominant time dependent
 258 model of *Soulsby et al.* [2012]; each summarized in the following.

259 Bedform evolution can be characterized with a time varying spectrum of bedform
 260 geometries defined by [*Traykovski, 2007*],

$$\frac{d\eta_{T07}(k)}{dt} = \frac{\eta_{eq}(k) - \eta_{T07}(k)}{T_{adj}(k)}, \quad (20)$$

261 where k is the associated bedform wavenumber ($2\pi/\lambda$), η_{eq} is the equilibrium ripple spec-
 262 tra modeled by a Gaussian distribution with inputs of a proposed equilibrium ripple height
 263 and ripple wavelength, and $T_{adj}(k)$ is an adjustment timescale for each wavenumber based
 264 on the wavenumber dependent cross sectional area of the bedform and the total bedform
 265 sediment flux, q [*Meyer-Peter and Muller, 1948*]. A numerical integration scheme results
 266 in a time series of wavenumber dependent ripple heights, where modeled η_{mT07} is found
 267 by integrating with respect to wavenumber (analogous to a significant wave height calcu-
 268 lation) as discussed previously, and modeled λ_{mT07} is defined by $2\pi/k$ of the peak spectral
 269 energy band for each time step. The model gives high skill predictions of ripple geometry
 270 in a predominantly wave environment, where the model skill is the correlation coefficient
 271 squared.

272 *Soulsby et al.* [2012] proposed a time-dependent bedform evolution model that uses
 273 a Shields parameter criterion to decide whether ripples are wave- or current- generated.
 274 A departure from equilibrium approach allows ripples to evolve based on an adjustment
 275 time scale. For a given bedform variable (either ripple wavelength or height) the model is
 276 defined by

$$\frac{dx_{SWM12}}{dt} = a(t) - b(t)x_{SWM12}(t), \quad (21)$$

277 where x_{SWM12} is either the modeled η_{mSWM12} or λ_{mSWM12} , and are found through numerical
 278 integration. Additionally, $a(t) = x_{eq}\beta/T_r$ and $b(t) = \beta/T_r + bio/T_b$, where x_{eq} is an equi-
 279 librium length and β is a rate of change parameter based on waves or current dominant
 280 forcing. T_r is a rate of change characteristic time scale that is equal to the wave period for
 281 wave forcing conditions and the time taken for an equilibrium ripple to be changed by the
 282 total bedload transport rate for current forcing. bio and T_b are a free parameter and a time
 283 scale related to biological degradation of the bedforms, respectively. The model has been
 284 shown to have high skill in prediction of wave dominant flow or current dominant flow
 285 bedforms of less than 0.5 m in wavelength; however it does not predict megaripples and
 286 does not account for combined wave-current flows.

3 Results

3.1 Observations of Bedform Geometry

Time series of hydrodynamic and bedform geometry observations are shown in Figures 2 and 3 for S1 and S2, respectively. S1 was deployed for a spring-neap-spring-neap-spring tidal cycle, including 4 storm events (day of year 278, 280, 287, 294). S2 was deployed for a neap-spring-neap tidal cycle with 3 storm events (day of year 278, 280, 287). At both locations the currents were strongly tidally influenced with stronger currents during flood tide, as the tidal flow runs parallel to the Delfland coast. Additionally, wave orbital velocities were tidally modulated due to waves breaking on an shore-parallel sandbar during low water, and more shoreward during high water (see Figure 1).

Bedform geometry was observed to vary substantially at each station over the period of investigation with a clear dependence on the type of hydrodynamic forcing (Figures 2 and 3). The hydrodynamic kinetic energy shaded by the fraction of energy due to waves ($E_{k_w}/E_{k_{wc}}$) highlights occurrences of current dominated flows (low $E_{k_w}/E_{k_{wc}}$), and wave dominated flows (high $E_{k_w}/E_{k_{wc}}$). During non-storm conditions semidiurnal peaks in the energy were associated with the tide as evident with low $E_{k_w}/E_{k_{wc}}$. At S2 larger wavelength bedforms corresponded with instances of increased flow, and occurred generally under current or combined flow dominant kinetic energy. However, observations at S1 showed that relatively large wavelength bedforms ($\lambda > 1$ m) can correspond with instances of large kinetic energy that was either current dominated or high wave energy dominated conditions (i.e. storms). Additionally, bedform steepness was generally characteristic of wave orbital ripple steepness ($\eta/\lambda \approx 0.16$) during wave energy dominated conditions, and dune steepness ($\eta/\lambda \approx 0.06$) during current energy dominated conditions [Wiberg and Harris, 1994; Fredsøe and Deigaard, 1992]. Figure 4 shows a truncated time series from Figure 2 to highlight the growth of one bedform over time with corresponding sonar images to show bed change.

3.2 Bedform Characterization

The distribution of the relative frequency of occurrence during each deployment of λ , η , and η/λ (Figure 5a-c for each site S1 and S2) shows that smaller wavelength bedforms occurred more often, and generally bedforms were in the range of the steepness of wave orbital ripples ($\eta/\lambda \approx 0.16$). However, the histogram of λ also shows that at each

318 site bedforms of wavelengths longer than 0.5 m occurred between 29-33% of the time,
 319 and bedforms with a steepness of less than that of wave orbital ripples occur approxi-
 320 mately 29-35% of the time. The observed bedforms were predominantly 2D, but dur-
 321 ing transition periods, bedforms could become 3D; the degree of three dimensionality is
 322 shown through the observed spread of dominant bedform orientation, as indicated with a
 323 shaded grey band (Figure 4).

324 Ripples observed in wave dominated environments are often characterized as either
 325 orbital ripples, suborbital ripples, and anorbital ripples [Clifton and Dingler, 1984; Wiberg
 326 and Harris, 1994]. The wavelength of orbital ripples scales with the orbital excursion of
 327 the waves. Anorbital ripples have a wavelength independent of orbital excursion and are
 328 thought to scale with the grain size. Suborbital ripples are some combination of the two
 329 regimes [Clifton and Dingler, 1984; Wiberg and Harris, 1994]. The Clifton and Dingler
 330 [1984] classification diagram is shown in Figure 6a overlaid with observations from S1
 331 and S2. The wave dominated bedforms, with large $E_{k_w}/E_{k_{wc}}$, generally were classified as
 332 orbital or slightly suborbital (falling on the dark grey bar in Figure 6a and are consistent
 333 with Clifton and Dingler [1984]). However, ripples with larger wavelengths correspond to
 334 periods with smaller $E_{k_w}/E_{k_{wc}}$ (Figure 6a blue shading) and fall in an unclassified region
 335 in Clifton and Dingler [1984]. The unclassified bedforms did not show evidence of be-
 336 ing relic (Figure 6a). Considering such attributes, we consider the bedforms that fall into
 337 this unclassified region by Clifton and Dingler [1984] as either combined wave-current or
 338 current dominant bedforms and were formed by the onset of strong currents.

339 Figure 6b shows the distribution of observed bedform wavelength as a function of
 340 $E_{k_w}/E_{k_{wc}}$, u_o , and U for both S1 and S2 sites. S1 and S2 were influenced strongly by
 341 tidal currents particularly with the occurrence of large U at relatively small u_o , that is,
 342 when wave-driven alongshore currents were weak (see Hay and Mudge [2005] Figure 11
 343 for a reference case with small tidal currents). Additionally, larger wavelength bedforms
 344 were shown to occur with large u_o and/or large U , indicating that bedforms may have
 345 been formed by waves, currents, and with combined wave-current forcing contributions,
 346 shown by the shading of $E_{k_w}/E_{k_{wc}}$.

3.3 Observations of Bedform Orientation

The bedforms at S1 and S2 were very dynamic. During transitional periods they were not aligned and instead were oriented over a range of directions between 5° and 90° . The bandwidth range was determined by the spacing between peaks in 2D spatial spectra and is indicated by a shaded grey band in Figure 7 and a shaded grey band on each 2D bathymetry plot (Figures 2-4). The bedforms generally did not align with the current or the wave direction, but rather a combination of both depending on flow dominance. The bedforms sometimes align with the wave direction when $E_{k_w}/E_{k_{wc}}$ was large, notably during low tide, and with the current direction when $E_{k_w}/E_{k_{wc}}$ was small (Figure 7b, c). However, the bedforms did not always align with the dominant flow direction (e.g. Figure 7b and c day of year 281.2).

Figure 8 shows the bedform orientation in relation to the current magnitude and direction, the wave orbital magnitude and direction, the bedform wavelength, and $E_{k_w}/E_{k_{wc}}$. The strongest correlation between the four metrics displayed is the bedform orientation in relation to the current magnitude (panel a). As bedforms became more current influenced (low $E_{k_w}/E_{k_{wc}}$) they not only increased in wavelength, but also tended to orient between 30° and 70° , approaching the direction of the prevailing flood tidal currents oriented toward the northeast (90° counterclockwise from shore-normal in Figure 1). However, the bedform orientation in relation to the orbital velocity magnitude did not show a clear trend (panel c), indicating that the magnitude of the waves did not have a large effect on bedform orientation.

When considering the bedform orientation in relation to the current and wave directions (Figure 8b, d), the bedforms generally did not align with either the current or wave direction. A root-mean-square-error range ($rmse_{range}$) analysis is used to determine how well the bedform orientation observations fit the wave and current directions. The metric is a modified $rmse$ calculation, where the difference between the measured and modeled orientations are set to zero if the wave or current direction falls anywhere within the bedform orientation bandwidth range, and the differences are calculated at the center of the range if the wave or current direction falls outside. Circular statistics were used to calculate the root-mean-square-error range. The bedform orientation root-mean-square-error range statistics (given in the caption of Figure 8) show that the bedform orientation was neither predominantly influenced by waves or currents. However, with respect to the root-

379 mean-square-error range analysis, the bedforms were more closely aligned with the wave
 380 direction than the current direction. Overall, the generally large root-mean-square-error
 381 range values indicate that the bedform orientation was not a function of the independent
 382 wave and current directions alone, but rather a concurrent combination [*Gallagher et al.*,
 383 1998; *Lacy et al.*, 2007].

384 4 Discussion

385 4.1 Time-evolving Bedform Geometry and the Sediment Continuity Equation

386 The relationship between hydrodynamic forcing and bedform wavelength over one
 387 tidal cycle is shown in Figure 4. In combined wave-current flows, the bedform wavelength
 388 increased with increasing duration of forcing demonstrating that λ at any instance in time
 389 was not only dependent on the present hydrodynamic forcing, but also on past hydrody-
 390 namic conditions over some lag time, τ . In wave dominant flows, the bedforms also grew
 391 in volume with increased duration of forcing; however, they generally reached an equi-
 392 librium wavelength, scaling with the wave statistics, where the combined flow bedforms
 393 never reached an equilibrium condition.

394 The bedform will grow/decay and/or migrate based on the position of peak transport
 395 with respect to the bedform crest. When the non-dimensional phase shift, δ_{x_b}/λ , is ± 0.25
 396 the bedform will only grow (+) or decay (-) in volume, when δ_{x_b}/λ is 0 the bedform will
 397 only migrate [*Nielsen*, 1992]. δ_{x_b}/λ was estimated by taking $t = dt$ and $x = 0$ since the
 398 non-dimensional phase shift is estimated with every measurement of bedform growth or
 399 decay and is estimated in position with respect to the bedform crest at $x = 0$. The bedform
 400 wavelength begins to increase with the onset of increases in $E_{k_{wc}}$. During this period the
 401 bedform grows and migrates, but when the bedform growth dominates δ_{x_b}/λ will be large,
 402 and when bedform migration dominates δ_{x_b}/λ will be close to zero (Figure 9 and Figure
 403 10). Generally, the largest periods of bedform growth or decay have small migrations, and
 404 the largest periods of migration have small growth or decay (Figure 10). The sediment
 405 transport increases with either increased migration or increased growth, and decays with
 406 decreased migration or decay in bedform volume. Additionally, q_b can be estimated from
 407 either (14) and (15), with each estimating similar magnitudes (Figure 9e).

408 The results of the continuity analysis given by (19) are shown as Figure 11 and 12.
 409 Figure 11 shows the observed change in bedform volume and the integral of the sediment

410 flux term calculated using (14) with three different methods (described below) to estimate
 411 the lag time for bedform growth, τ . The bedform volume was calculated by taking the av-
 412 erage cross section of the ripple profile in the direction of the bedform orientation, and
 413 then used with the measured ripple wavelength from the 2D spectra to find the mean bed-
 414 form volume for each time step.

415 To find the bedform adjustment time, τ , the first method sets $\tau = dt$, one sam-
 416 ple time step (for S1 $dt = 20$ min. and for S2 $dt = 2$ hr.; denoted τdt in Figures 11 and
 417 12). The second method sets $\tau = \tau_{zc}$, or the adjustment time found with observations of
 418 bedform growth or decay by the time between subsequent upward and downward zero-
 419 crossings in $d\Lambda_b/dt$. An upward zero-crossing indicates the initiation of bedform growth,
 420 and a downward zero-crossing indicates the start of bedform decay. The time between up-
 421 ward to downward zero-crossings represents the adjustment time that the bedform under-
 422 went to reach its largest volume before it started to decay. The time between downward to
 423 upward zero-crossings represents the adjustment time for bedform decay. Depending upon
 424 the flow forcing condition, τ_{zc} will change. If the bedform reaches an equilibrium condi-
 425 tion with the flow, and stops growing or decaying, the lag time was set to dt . An example
 426 of an individual bedform growing over time at S1 is shown in Figure 4. In this case the
 427 bedform adjusted to the flow field for approximately 2.4 hours (0.1 days) before its vol-
 428 ume began to decay; thus for this case $\tau_{zc} = 2.4$ hours. The observed bedform adjustment
 429 time using the zero-crossing method showed that within wave dominant conditions, the
 430 bedform adjustment time was fairly quick. Within 20 minutes to 1 hour the bedforms be-
 431 gan to come into equilibrium with the flow field; however, with the addition of currents,
 432 the adjustment time became much longer, approximately 2.5 hours to 6 hours and the bed-
 433 forms may have never adjusted into equilibrium with the flow forcing. The third method
 434 to find τ uses $\tau = \frac{nm\lambda}{2q_b}$ [Traykovski, 2007]. The method assumes that the sediment flux
 435 during bedform growth is uniform with respect to time. Since (19) estimates the change
 436 in bedform volume as a function of the sediment transport, it is viable even through qui-
 437 escent conditions. However, with the dynamic qualities of this assumption has not been
 438 evaluated in such a dynamic environment.

439 Observations captured many instances of bedform building and decay over time (e.g.
 440 Figure 4). When $\tau = dt$, (19) greatly underestimates the change in bedform volume, es-
 441 pecially for S1 where dt is much shorter (Figure 11 and 12). The under estimation is es-
 442 pecially apparent during instances of increased changes in bedform volume, suggesting

443 that bedform building or decay is a time dependent process. Additionally, at S1, τ was
 444 estimated using the bedform zero-crossing method. However, at S2, the bedform zero-
 445 crossing method could not be used because the sampling rate between subsequent sonar
 446 images was too slow to capture bedform building. The method to estimate the bedform
 447 adjustment time from *Traykovski* [2007] was applied at both S1 and S2.

448 At both S1 and S2, it is clearly evident that (19) has higher skill using a variable τ .
 449 Figure 11b and Figure 12 demonstrates that τ estimated directly from the bedform zero-
 450 crossing method ($rmse = 0.019 \text{ m}^3/\text{m}$, $r^2 = 0.86$ for S1) or calculated using $\tau = \frac{n\eta\lambda}{2qb}$
 451 ($rmse = 0.021 \text{ m}^3/\text{m}$, $r^2 = 0.64$ for S1 and S2) represents the range of measured bedform
 452 volumes much better than $\tau = dt$ ($rmse = 0.029 \text{ m}^3/\text{m}$, $r^2 = 0.22$ for S1 and S2).

453 **4.2 Existing Time-Dependent Bedform Geometry Model Comparisons**

454 Previous bedform geometry work primarily focuses on approximating bedform ge-
 455 ometry (λ and η) from the overlying flow field. In our effort instead of bedform volume
 456 (Λ_b) as was predicted with the sediment continuity equation in the previous section. The
 457 leading time dependent bedform geometry models for prediction of bedform wavelength
 458 and height are *Traykovski* [2007] and *Soulsby et al.* [2012]. Each model was evaluated us-
 459 ing the data collected at S1 and S2 for both the entire dataset as well as a subset of the
 460 data that represents data from which the model was developed (Figure 13).

461 The *Traykovski* [2007] model is formulated for waves only, and with smaller orbital
 462 ripples it performed with twice the r^2 . Their model $rmse$ decreased by 2/3 or better for
 463 both λ and η when compared with the full dataset, which includes combined flow and
 464 current generated bedforms (Figure 13a, c). However, the concept behind the adjustment
 465 timescale, T_{adj} , in the *Traykovski* [2007] model is valid for both wave and current gener-
 466 ated bedforms (as shown in Figure 12).

467 The *Soulsby et al.* [2012] model is applicable to either wave or current generated
 468 bedforms, but it generally fails to predict megaripple scale bedforms. If the model is used
 469 to predict bedforms with wavelengths less than 0.5 m (regardless of flow dominance),
 470 the model r^2 stays the same, but the model $rmse$ decreases by 2/3 or better, suggesting
 471 a model bias. The *Soulsby et al.* [2012] model may poorly predict larger volume bedforms
 472 partially because it excludes the effects of combined flows that are prevalent at S1 and S2.
 473 Additionally, the estimated equilibrium bedform geometry model used by *Soulsby et al.*

474 [2012] considerably under-predicts ($\lambda_{eq} \sim 0.3$ m) the observed bedform wavelengths (λ
 475 = 1-2.5 m) during combined flows. Finally, in *Soulsby et al.* [2012] the criterion distin-
 476 guishing between wave or current generated bedforms is based on the Shields parameter,
 477 and depending on the approximation used for bed stress, under predicts mobility during
 478 combined flow conditions at the S1 and S2 sites.

479 The adjustment characteristic to an equilibrium length scale in *Traykovski* [2007] and
 480 *Soulsby et al.* [2012] seems reasonable; however, in practice may hinder the model skill
 481 (especially during combined flow conditions). The equilibrium geometry parameterizations
 482 may not be appropriate to all bedform generation conditions, especially combined wave-
 483 current bedforms. Additionally, the transition from wave generated to current generated is
 484 abrupt in the *Soulsby et al.* [2012] model, and does not allow for combined flow bedform
 485 generation.

486 Although these models have some limitations, their incorporation of time depen-
 487 dent growth is relevant to bedform building, even in combined wave-current flows. In our
 488 dataset, although wave dominated bedforms at times come into equilibrium with the wave
 489 conditions, the combined flow bedforms, never actually came into equilibrium with the
 490 flow forcing. The departure from equilibrium theory could be an explanation for the in-
 491 ability for bedform geometry models such as *Traykovski* [2007] and *Soulsby et al.* [2012]
 492 to predict bedform wavelength and height in combined flows. Although both of these
 493 models are time dependent, they also are based on an equilibrium approach. Equilibrium
 494 theory may not be representative of the physics of combined flow bedform growth, or at
 495 least, present equilibrium theory may not be consistent with the stability condition of com-
 496 bined wave-current bedforms.

497 **5 Conclusions**

498 Observations of bedform response to wave, current, and high energy combined wave-
 499 current dominant flows are presented. The observations capture both ripple and megarip-
 500 ple response to hydrodynamic conditions consisting of wave forcing plus strong currents
 501 (>0.5 m/s) collected within and near the surf zone. Dynamic bedform geometry transi-
 502 tions in response to shifts in flow conditions are resolved. Observations show that bedform
 503 volume - when exposed to current and combined wave-current forcing - continuously build
 504 until the flow changes.

505 Bedform transformation and growth are shown to be a highly time dependent sed-
506 iment transport process. With hydrodynamic transitions, the bedform scaling did not re-
507 spond immediately; instead, the bedform adjustment lagged behind in response to new
508 forcing condition. Within wave dominant conditions, the bedform adjustment time was
509 fairly quick; within 20 minutes to 1 hour the bedforms began to come into equilibrium
510 with the flow field. However, when strong currents were present, the adjustment time be-
511 came much longer, ranging between 2.5 hours to 6 hours and the bedforms never actually
512 came into complete equilibrium with the flow forcing. The departure from equilibrium
513 conditions captured in this dataset may be responsible for the inability of existing bed-
514 form geometry models to predict bedform wavelength and height in the measured com-
515 bined flows. Demonstrating that current equilibrium theory may not be representative of
516 combined flow bedform growth or, at least not consistent with the stability condition for
517 combined wave-current bedforms.

518 Aside from our dynamic set of observations of bedform response to combined wave-
519 current flows, our effort demonstrates that bedform volume at any given time was depen-
520 dent on both the sediment transport rate and the time duration that the bedform was ex-
521 posed to the flow field. Measured changes in bedform volume were additionally shown
522 to be characterized with the sediment continuity equation, or Exner equation, integrated
523 over the bedform adjustment time of growth, which to our knowledge is a new contribu-
524 tion that builds upon past efforts. In addition, our effort contributes expressions for the
525 fully unsteady bedform migration rate, growth rate, sediment transport phase shift, and
526 change in volume. The sediment continuity equation while accounting for bedform adjust-
527 ment/growth times may be a viable method for temporal and spacial morphologic change
528 predictions of bedforms, especially in combined wave-current flows and with bedforms of
529 a larger scale.

530 **Acknowledgments**

531 We would like to acknowledge the team of graduate students, faculty members, and tech-
532 nicians, from multiple countries and institutions who helped collect these data, with a
533 special thanks to Jon Hunt from UNH. We would especially like to thank Prof. Dano
534 Roelvink, who significantly contributed to the theoretical development behind this work,
535 as well as the thoughtful comments of an anonymous reviewer. Additionally, we would
536 like to thank the many departments and foundations who funded in this work. MegaPEX

537 was funded through NWO grant 12686, Nature Coast, and ERC Advance grant 91206,
538 NEMO. The UNH contribution to MegaPEX was funded by the PADI Foundation. MEW
539 was supported by the U.S. Department of Defense NDSEG fellowship. DLF was funded
540 by NSF grant number 1135026. TCL was funded under ONR contract number N00014-
541 14-1-0557. MdS was supported by NWO grant 15058, Feeding Starved Coasts by Mor-
542 phological Diffusivity. JC was supported under base funding to the U.S. Naval Research
543 Laboratory from the Office of Naval Research. Data from MegaPEX can be found at
544 data.4tu.nl/repository/collection:zandmotor

545 **References**

- 546 Alamo, J. C., and J. Jimenez (2003), Spectra of very large anisotropic scales in turbulent
547 channels, *Physics of Fluids Letters*, *15*(6).
- 548 Austin, M. J., G. Masselink, T. J. O'Hare, and P. E. Russell (2007), Relaxation time ef-
549 fects of wave ripples on tidal beaches, *Geophysical Research Letters*, *34*.
- 550 Becker, J. M., Y. L. Firing, J. Aucan, R. Holman, M. Merrifield, and G. Pawlak (2007),
551 Video-based observations of nearshore sand ripples and ripple migration, *Journal of*
552 *Geophysical Research*, *112*.
- 553 Clifton, H. E., and J. R. Dingle (1984), Wave-formed structures and paleoenvironmental
554 reconstruction, *Marine Geology*, *60*, 165–198.
- 555 Davis, J. P., D. J. Walker, M. Townsend, and I. R. Young (2004), Wave-formed sed-
556 iment ripples: Transient analysis of ripple spectral development, *J. Geophys. Res.*,
557 *109*(C07020, doi:10.1029/2004JC002307), 1–15.
- 558 Doucette, J. S., and T. O'Donoghue (2006), Response of sand ripples to change in oscilla-
559 tory flow, *Sedimentology*, *53*, 581–596.
- 560 Fredsøe, J. (1984), Turbulent boundary layer in wave-current motion, *J. Hydraul. Eng.*,
561 *110*(8).
- 562 Fredsøe, J., and R. Deigaard (1992), *Mechanics of coastal sediment transport*, World Sci-
563 entific.
- 564 Gallagher, E. L. (2003), A note on megaripples in the surf zone: evidence for their rela-
565 tion to steady flow dunes, *Marine Geology*, *193*, 171–176.
- 566 Gallagher, E. L., S. Elgar, and E. B. Thornton (1998), Megaripple migration in a natural
567 surf zone, *Letters to Nature*, *394*.

- 568 Ganju, N. E., and C. R. Sherwood (2010), Effect of roughness formulation on the perfor-
569 mance of a coupled wave, hydrodynamic, and sediment transport model, *Ocean Model-*
570 *ing*, 33, 299–313.
- 571 Grant, W. D., and O. S. Madsen (1979), Combined wave and current interaction with a
572 rough bottom, *J. Geophys. Res.*, 84(C4), 1797–1808.
- 573 Hay, A. E., and T. Mudge (2005), Principal bed states during sandyduck97: Occurrence,
574 spectral anisotropy, and the bed state storm cycle, *J. Geophys. Res.*, 110(C03013,
575 doi:10.1029/2004JC002451), 1–18.
- 576 Lacy, J. R., D. M. Rubin, H. Ikeda, K. Mokudai, and D. M. Hanes (2007), Bed forms cre-
577 ated by simulated waves and currents in a large flume, *Journal of Geophysical Research*,
578 112.
- 579 Larsen, S. M., B. Greenwood, and R. Aagaard (2015), Observations of megaripples in the
580 surf zone, *Marine Geology*, 364.
- 581 Lesser, G. R., J. A. Roelvink, T. M. van Kester, and G. S. Stelling (2004), Development
582 and validation of a three-dimensional morphological model, *Coastal Engineering*, 51,
583 883–915.
- 584 Li, M. Z., and C. L. Amos (1998), Predicting ripple geometry and bed roughness under
585 combined waves and currents in a continental shelf environment, *Continental Shelf Re-*
586 *search*, 18, 941–970.
- 587 Madsen, O., Y. Poon, and H. Graber (1988), Spectral wave attenuation by bottom friction:
588 Theory, *Coastal Engineering, Proceedings of the 21st Conference Am. Soc. Civ. Eng. New*
589 *York, 1*.
- 590 Maier, I., and A. E. Hay (2009), Occurrence and orientation of an orbital ripples in near-
591 shore sands, *Journal of Geophysical Research*, 114.
- 592 Meyer-Peter, E., and R. Muller (1948), Formulas for bed-load transport, in *Report on the*
593 *Second Meeting of the International Association for Hydraulic Structures Research*, pp.
594 39–64, Stockholm.
- 595 Nelson, T. R., and G. Voulgaris (2015), A spectral model for estimating temporal and spa-
596 tial evolution of rippled seabeds, *Ocean Dynamics*, 65, 155–171.
- 597 Nielsen, P. (1992), *Coastal bottom boundary layers and sediment transport*, World Scien-
598 tific.
- 599 Passchier, S., and M. G. Kleinhan (2005), Observations of sand waves, megaripples, and
600 hummocks in the dutch coastal area and their relation to currents and combined flow

- 601 conditions, *J. Geophys. Res.*, *110*.
- 602 Penko, A., J. Calantoni, and B. T. Hefner (2017), Modeling and observations of sand rip-
603 ple formation and evolution during trex13, *Journal of Oceanic Engineering*.
- 604 Radermacher, M., M. A. de Schipper, C. Swinkels, J. H. MacMahan, and A. J. Reniers
605 (2017), Tidal flow separation at protruding beach nourishments, *Journal of Geophysical*
606 *Research: Oceans*, *122*, 63–79.
- 607 Roelvink, D., and A. J. H. M. Reniers (2011), *A Guide to Modeling Coastal Morphology*,
608 vol. 12, WSPC.
- 609 SeaBeam (2000), Multibeam sonar theory of operation, *Tech. rep.*, L3 Communications of
610 SeaBeam Instruments.
- 611 Smith, D., and J. F. A. Sleath (2005), Transient ripples in oscillatory flows, *Cont. Shelf*
612 *Res.*, *25*, 485–501.
- 613 Soulsby, R., and S. Clarke (2005), Bed shear-stresses under combined waves and currents
614 on smooth and rough beds, *Report TR 137*, HR Wallingford.
- 615 Soulsby, R. L., R. J. S. Whitehouse, and K. V. Marten (2012), Prediction of time-evolving
616 sand ripples in shelf seas, *Continental Shelf Res.*, *38*, 47–62.
- 617 Stive, M. J. F., M. A. de Schipper, A. P. Luijendijk, S. G. J. Aarninkhof, C. van Gelder-
618 Maas, J. S. M. van Thiel de Vries, S. de Vries, M. Henriquez, S. Marx, and R. Ranas-
619 inghe (2013), A new alternative to saving our beaches from sea-level rise: The sand
620 engine., *J. Coastal Research*, *29*(5).
- 621 Testik, F. Y., S. I. Voropayev, and H. J. S. Fernando (2005), Adjustment of sand ripples
622 under changing water waves, *Physics of Fluids*, *17*.
- 623 Traykovski, P. (2007), Observations of wave orbital scale ripples and a nonequilibrium
624 time-dependent model, *J. Geophys. Res.*, *112*(C06026), doi:10.1029/2006JC003,811.
- 625 Traykovski, P., A. E. Hay, J. D. Irish, and J. F. Lynch (1999), Geometry, migration, and
626 evolution of wave orbital ripples at leo-15, *J. Geophys. Res.*, *104*(C1), 1505–1524.
- 627 Wengrove, M. E., D. L. Foster, M. A. de Schipper, and T. C. Lippmann (2017), Wave and
628 current ripple formation and migration during storms, *Proceedings of Coastal Dynamics*
629 *2017*, (129).
- 630 Wiberg, P. L., and C. K. Harris (1994), Ripple geometry in wave-dominated environments,
631 *Journal of Geophysical Research*, *99*.
- 632 Wikramanayake, P. N., and O. S. Madsen (1994), Calculation of movable bed friction fac-
633 tors, *Technical report for us army corps of engineers*, Massachusetts Institute of Technol-

634 ogy.

635 **Figure 1.** a) September 2014 bathymetry of Sand Engine mega-nourishment, Delfland, The Netherlands. b)
636 Inset marked on panel a shows the sampling locations S1 and S2 indicated with white circles. Site S1 is close
637 to the shoreline, and site S2 is close to the shore-parallel sandbar. The coordinate system used in this research
638 is defined relative to the low tide shoreline, where shore parallel (alongshore) is y with $+y$ being toward the
639 Northeast, and shore normal (cross shore) is x with $+x$ directed offshore. c) and d) Instrument array. Station
640 S1 included an Imagenex 881a pencil beam sonar located 0.7 m from the bed and an ADCP located 0.4 m
641 from the bed, and station S2 included an Imagenex 881a pencil beam sonar 1 m from the bed and an ADV 1 m
642 from the bed.

643 **Figure 2.** Time series of observations at S1, where panel a) shows depth (h), b) shows amplitude of wave
 644 orbital velocity, u_o , in grey and mean velocity, U , in black, c) shows maximum kinetic energy, $E_{k_{wc}}$ shaded
 645 by fraction of kinetic energy due to waves, d) shows ripple wavelength, λ , e) and shows ripple steepness, η/λ .
 646 The vertical dashed lines in panels d and e indicate occurrences of local bathymetries shown as panels f-h.
 647 Panels f-h) show 2D bathymetries, where y is shore parallel, and x is shore-normal, with $-x$ directed onshore,
 648 and is shaded by bedform height. Finally, dashed lines and shaded overlay in panels f-h indicate bedform
 649 orientation and orientation uncertainty, respectively.

650 **Figure 3.** Time series of observations at S2, where panel a) shows depth (h), b) shows amplitude of wave
 651 orbital velocity, u_o , in grey and mean velocity, U , in black, c) shows maximum kinetic energy, $E_{k_{wc}}$ shaded
 652 by fraction of kinetic energy due to waves, d) shows ripple wavelength, λ , e) and shows ripple steepness, η/λ .
 653 The vertical dashed lines in panels d and e indicate occurrences of local bathymetries shown as panels f-h.
 654 Panels f-h) show 2D bathymetries, where y is shore parallel, and x is shore-normal, with $-x$ directed onshore,
 655 and is shaded by bedform height. Finally, dashed lines and shaded overlay in panels f-h indicate bedform
 656 orientation and orientation uncertainty, respectively.

657 **Figure 4.** Time series of observations at S1 for one tidal cycle, where panel a) shows depth (h), b) shows
 658 amplitude of wave orbital velocity, u_o , in grey and mean velocity, U , in black, c) shows maximum kinetic
 659 energy, $E_{k_{wc}}$ shaded by fraction of kinetic energy due to waves, and d) shows ripple wavelength, λ . The ver-
 660 tical dashed lines in panel d indicate occurrences of local bathymetries shown as panels e-j. Panels e-j) show
 661 2D bathymetries, where y is shore parallel, and x is shore-normal, with $-x$ directed onshore, and is shaded by
 662 bedform height. Finally, dashed lines and shaded overlay in e-j indicate bedform orientation and orientation
 663 uncertainty, respectively.

664 **Figure 5.** Histograms of bedform a) wavelength (λ), b) amplitude (η), and c) steepness (η/λ) at both
 665 stations, where S1 is in black and S2 is in grey.

666 **Figure 6.** Bedform classification scatter plot diagrams. Panel a) shows the *Clifton and Dingle* [1984]
 667 classification diagram (dark gray are classified as orbital ripples and white as anorbital ripples, with the region
 668 in-between classified as suborbital ripples) overlaid with observations from S1 and S2, shaded by fraction
 669 of kinetic energy due to waves. Panel b) shows the distribution of observed bedform wavelengths based on
 670 orbital velocity and current velocity flow contributions, shaded by fraction of energy due to waves, where the
 671 marker size indicates bedform wavelength (with larger markers indicating larger λ as shown at the top of the
 672 panel).

673 **Figure 7.** Observed bedform direction and concurrent flow directions. Panel a) shows a time series of depth
 674 at S1. Panel b) S1 and c) S2, show time series of range of observed bedform orientation colored by fraction
 675 of kinetic energy due to waves (circles with range bars), observed current direction (black dots), and observed
 676 wave direction (thin black line).

677 **Figure 8.** Observed bedform directions plotted against a) current magnitude, b) current direction
 678 [$rmse_{range} = 40^\circ$], c) wave orbital magnitude, d) wave orbital direction [$rmse_{range} = 23^\circ$]. $rmse$ is calcu-
 679 lated between the observed bedform range and the model as described in the text. Markers are colored by
 680 the fraction kinetic of energy due to waves and the size of the marker scales with the bedform wavelength as
 681 indicated in the bottom of panel d.

682 **Figure 9.** Time series of indicators for bedform growth, decay, and migration. Panel a) shows the wave-
 683 current energy time series colored by fraction of kinetic energy due to waves at S1. Panel b) shows a short
 684 time series of bedform wave length (o) and height (●). Panel c) shows the bedform growth/decay rate in red
 685 and the bedform migration rate in blue. Panel c) shows the non-dimensional phase offset between the sedi-
 686 ment transport and bed shape, when δ_{x_b}/λ is positive the bedform will grow, negative will decay, and 0 will
 687 migrate. Panel e) shows the bedload sediment transport estimated with equations (14) (blue) and (15) (red).

688 **Figure 10.** Scatter plot of bedform growth/decay and migration rate, colored by the non-dimensional phase
 689 offset between the sediment transport and bed shape, δ_{x_b}/λ is estimated with (17). When δ_{x_b}/λ is positive
 690 the bedform will grow, negative will decay, and 0 will migrate.

691 **Figure 11.** Time series of bedform volume represented by the sediment continuity equation. Panel a) shows
 692 the wave-current energy time series colored by fraction of kinetic energy due to waves at S1. Panel b) shows
 693 a short time series of $\Delta\Lambda_b$, where the thick grey line is the RHS of (19) and the markers represent the LHS of
 694 (19) using various approximations of the bedform lag time, τ , estimated as follows. The black \times use a $\tau = dt$,
 695 the blue \circ use a τ directly estimated from the bedform zero-crossing method, and the red \bullet use a τ estimated
 696 from ($\tau = \frac{n\eta\lambda}{2q_b}$).

697 **Figure 12.** Scatter plot of the change in bedform unit volume vs. the time integrated transport (LHS vs.
 698 RHS of (19)) for the full data set collected at a) S1, and b) S2. The change in bedform volume (x axis) is
 699 plotted against the time integrated sediment flux using different approximations of the bedform lag time, τ (y
 700 axis). The black \times use a $\tau = dt$, the blue \circ use a τ directly estimated from the bedform zero-crossing method,
 701 and the red \bullet use a τ estimated from ($\tau = \frac{n\eta\lambda}{2q_b}$). The solid black line is a 1 to 1 line. For the bedform zero-
 702 crossing method, $rmse = 0.019 \text{ m}^3/\text{m}$, $r^2 = 0.86$ for S1. For $\tau = \frac{n\eta\lambda}{2q_b}$, $rmse = 0.021 \text{ m}^3/\text{m}$, $r^2 = 0.64$. For
 703 $\tau = dt$, $rmse = 0.029 \text{ m}^3/\text{m}$, $r^2 = 0.22$.

704 **Figure 13.** Observed vs. modeled bedform λ (panels a) and b)) and η (panels c) and d)) for site S1 in \times
 705 and S2 in \circ . The grey markers show all data, and the black markers show the subset of data that the model
 706 was designed and tested on. a,c) plot the *Traykovski* [2007] model from (20), where the data in black are for
 707 wave dominant flows only, b,d) plot the *Soulsby et al.* [2012] model from (21), where the data in black are for
 708 bedforms less than 0.5 m in wavelength only. The model $rmse$ and r^2 are indicted in the lower right corner of
 709 each panel.

Figure 1.

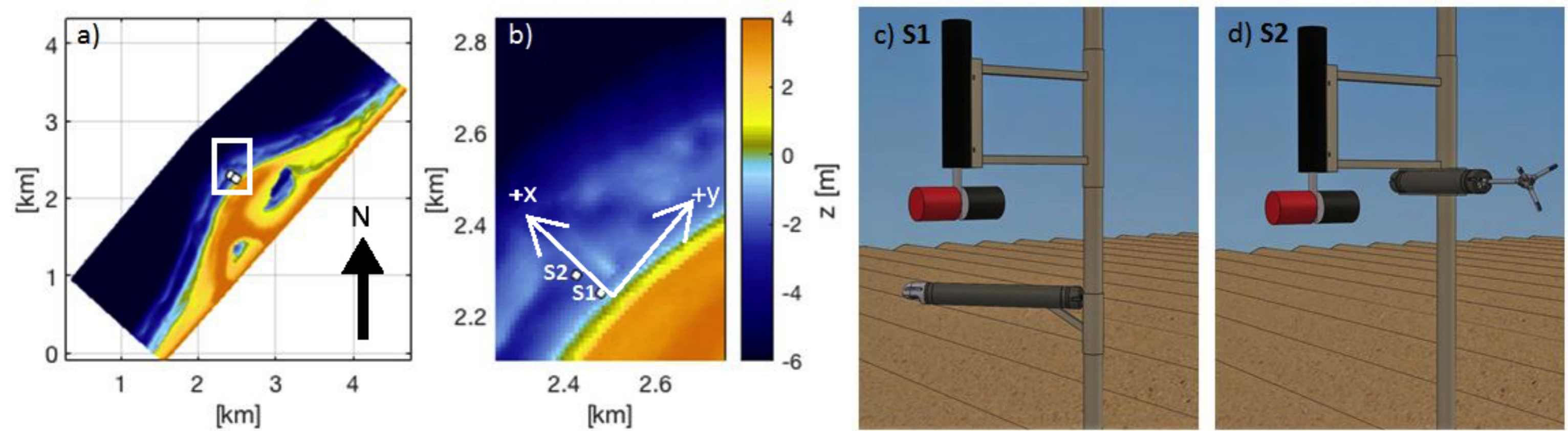


Figure 2.

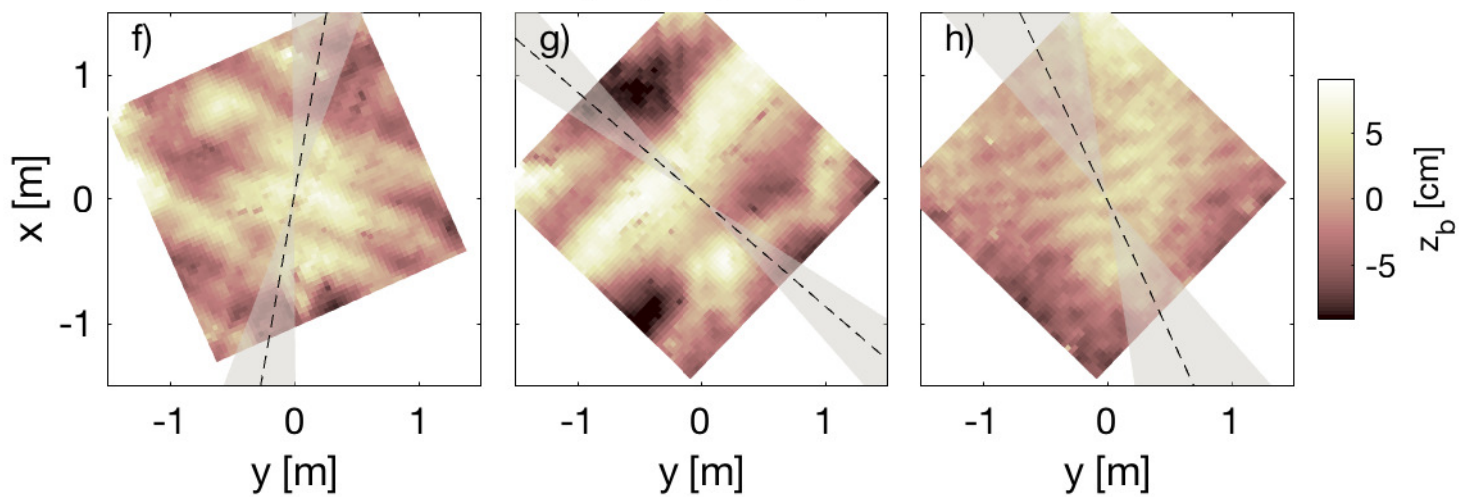
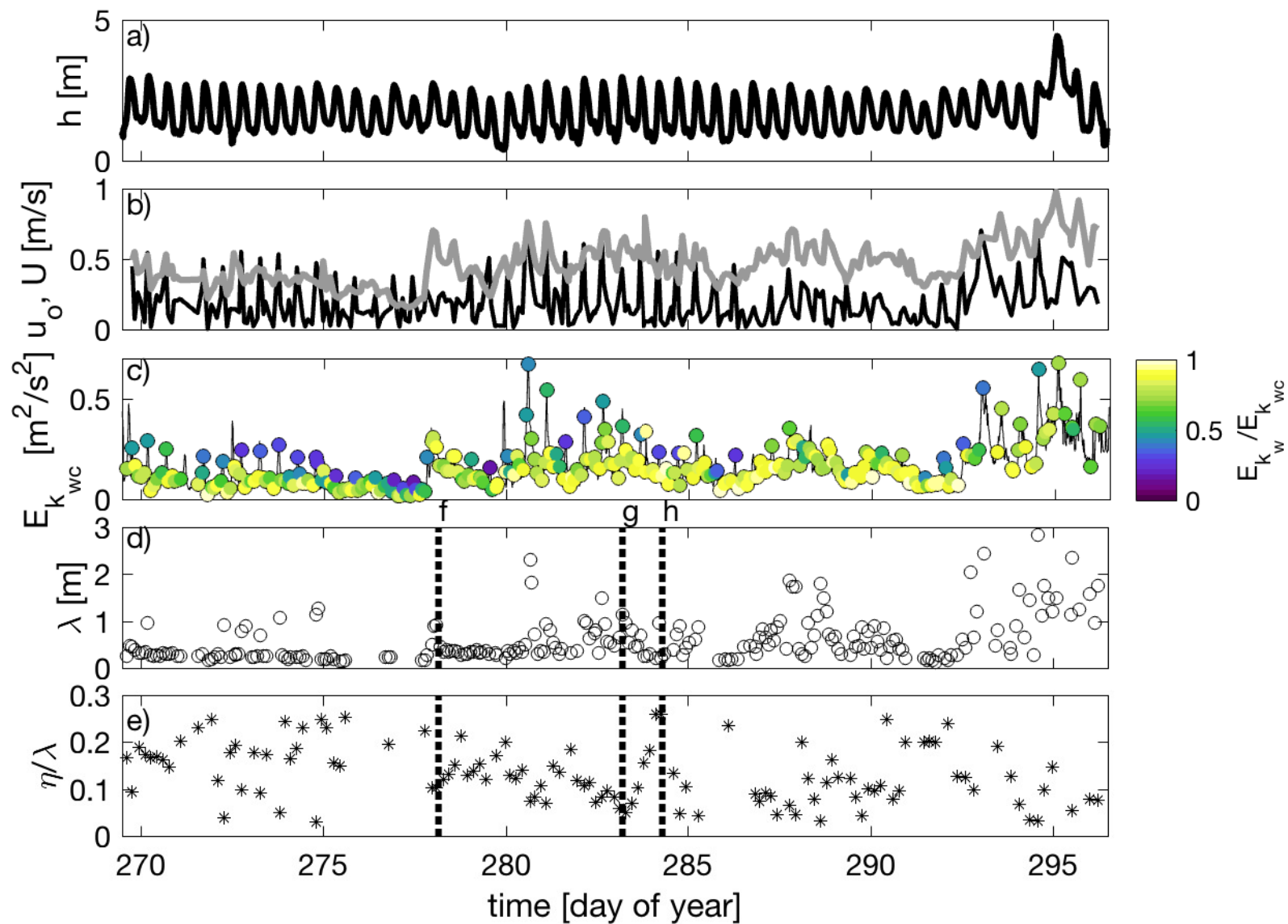


Figure 3.

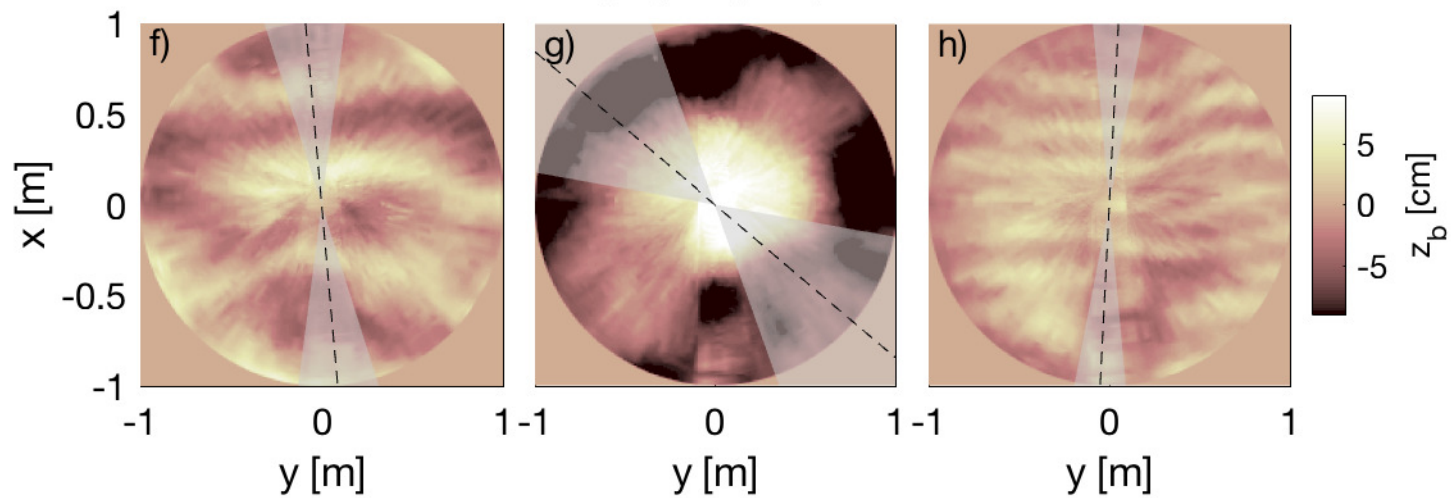
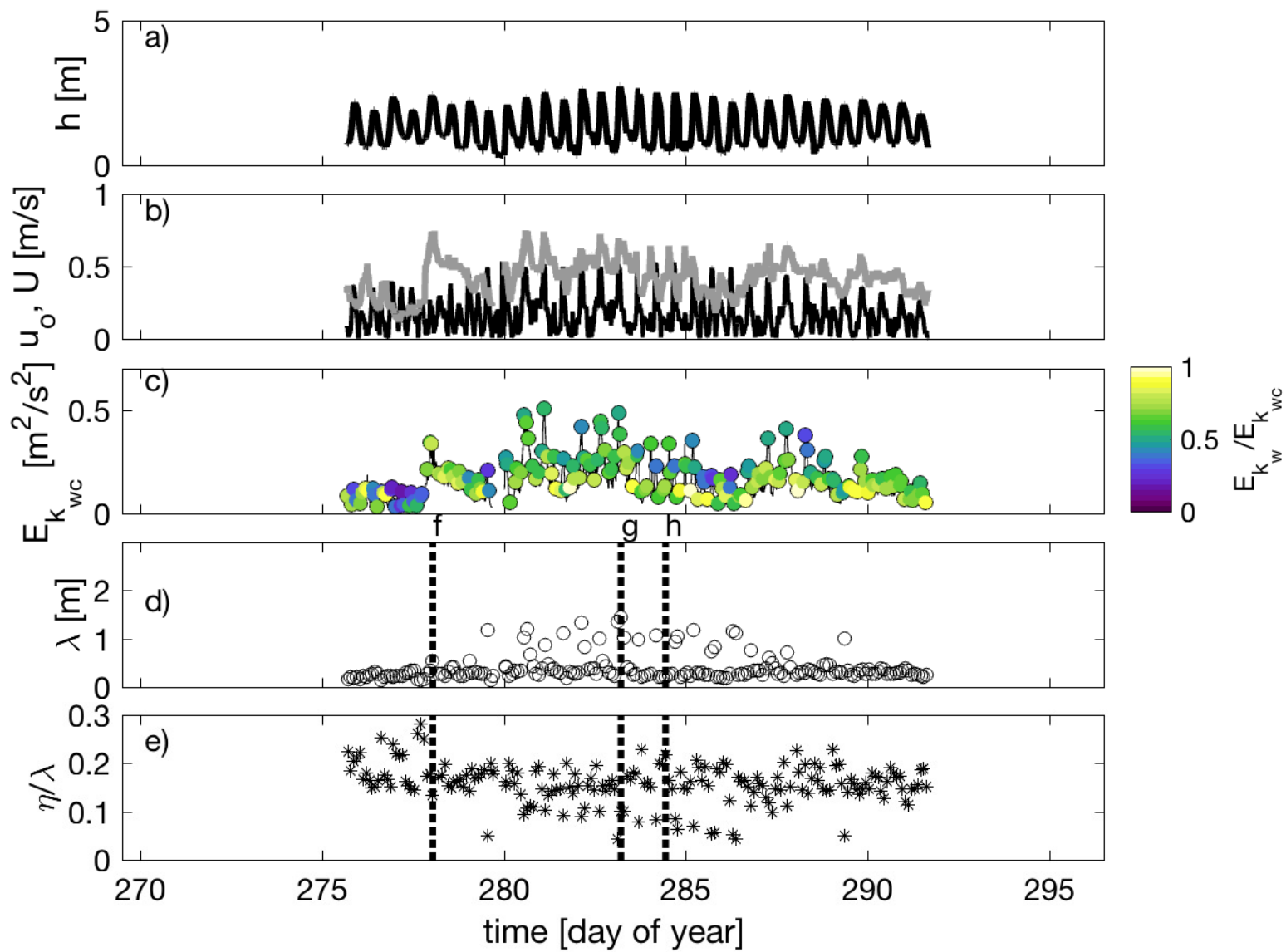


Figure 4.

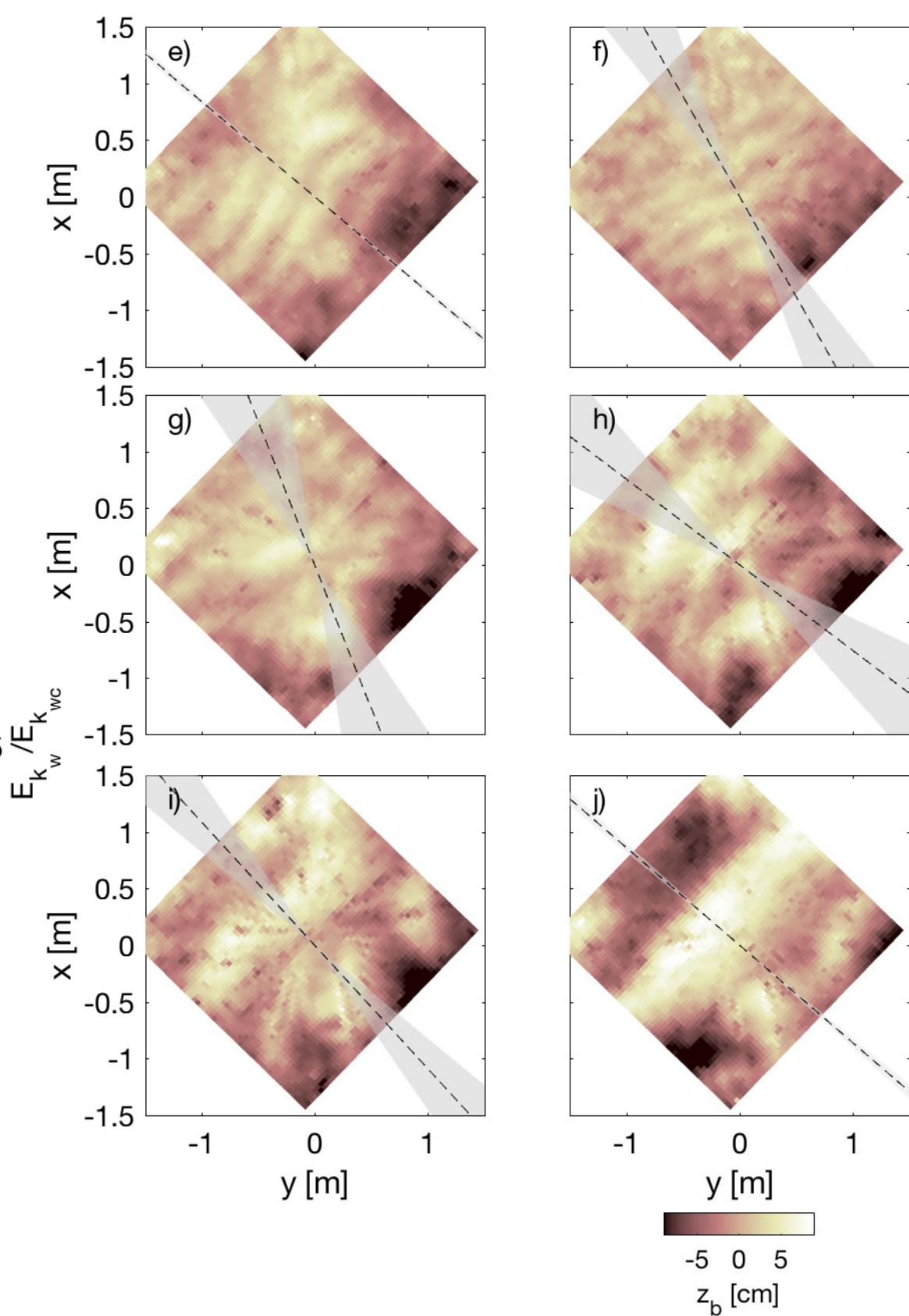
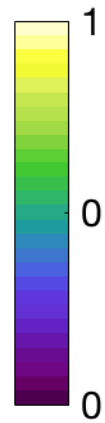
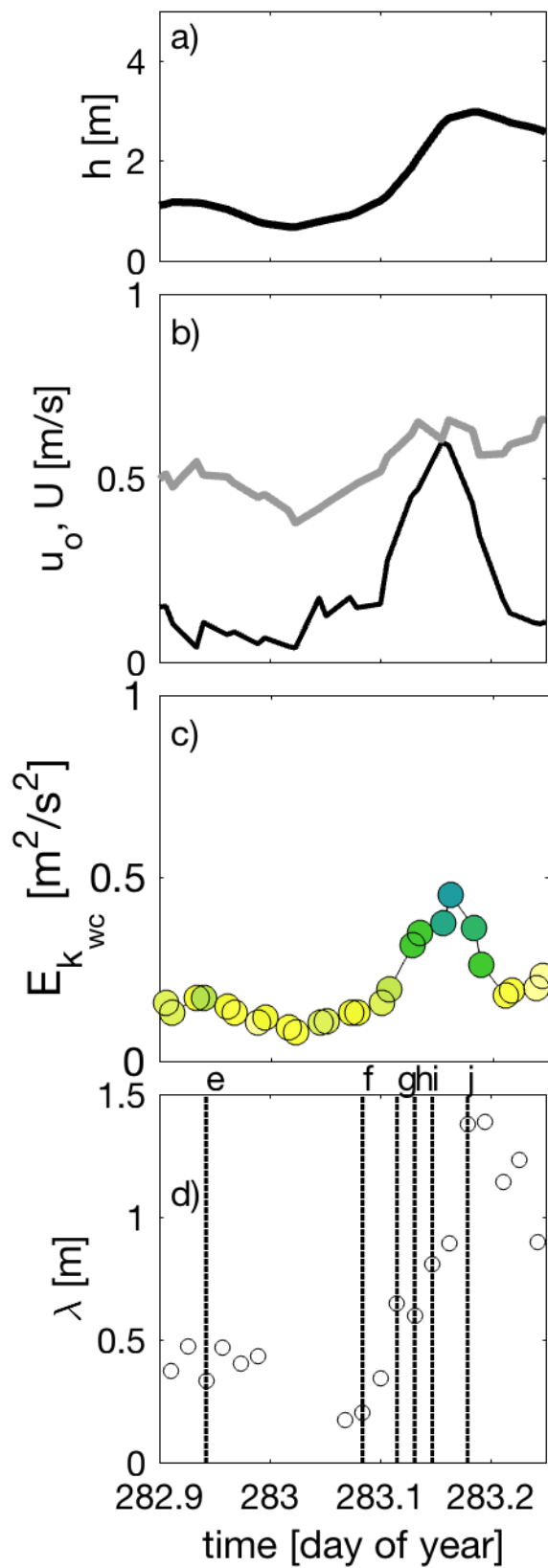


Figure 5.

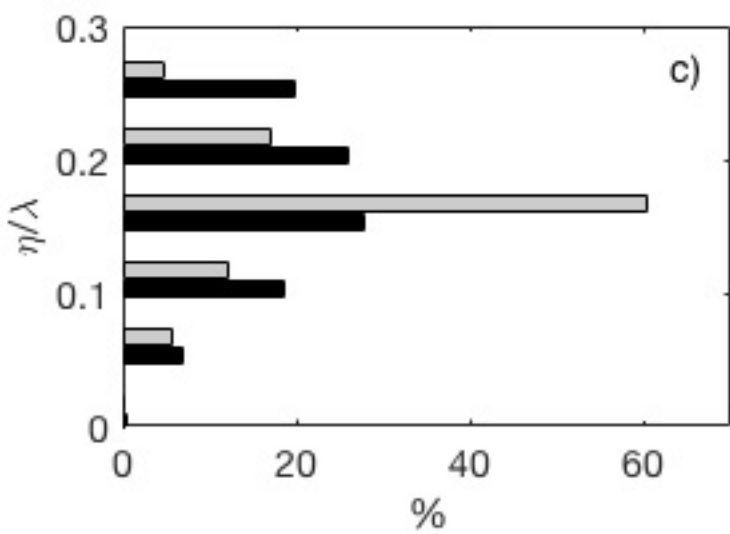
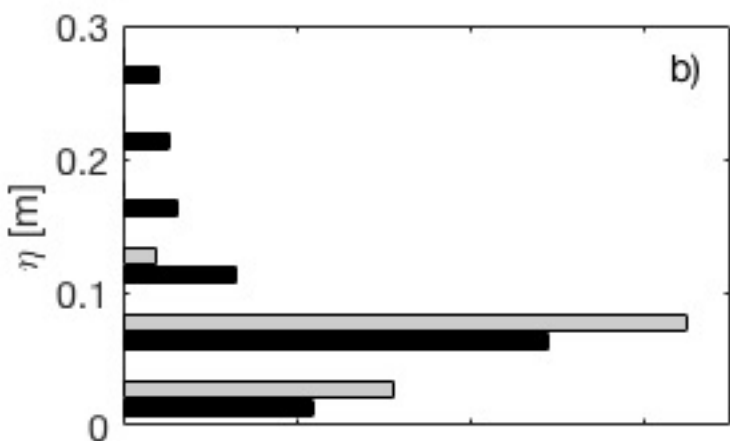
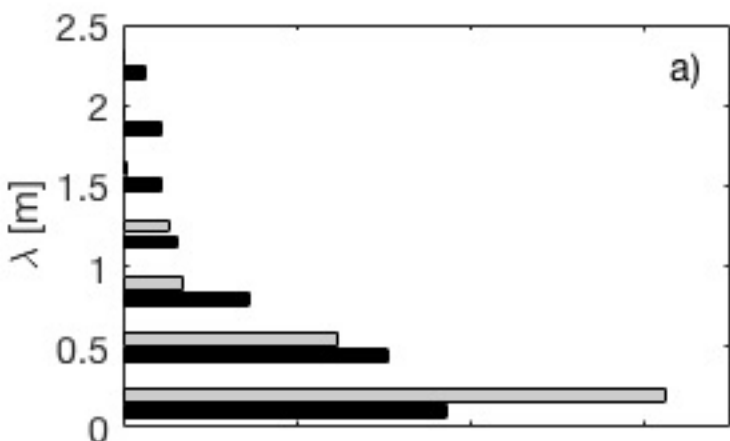


Figure 6.

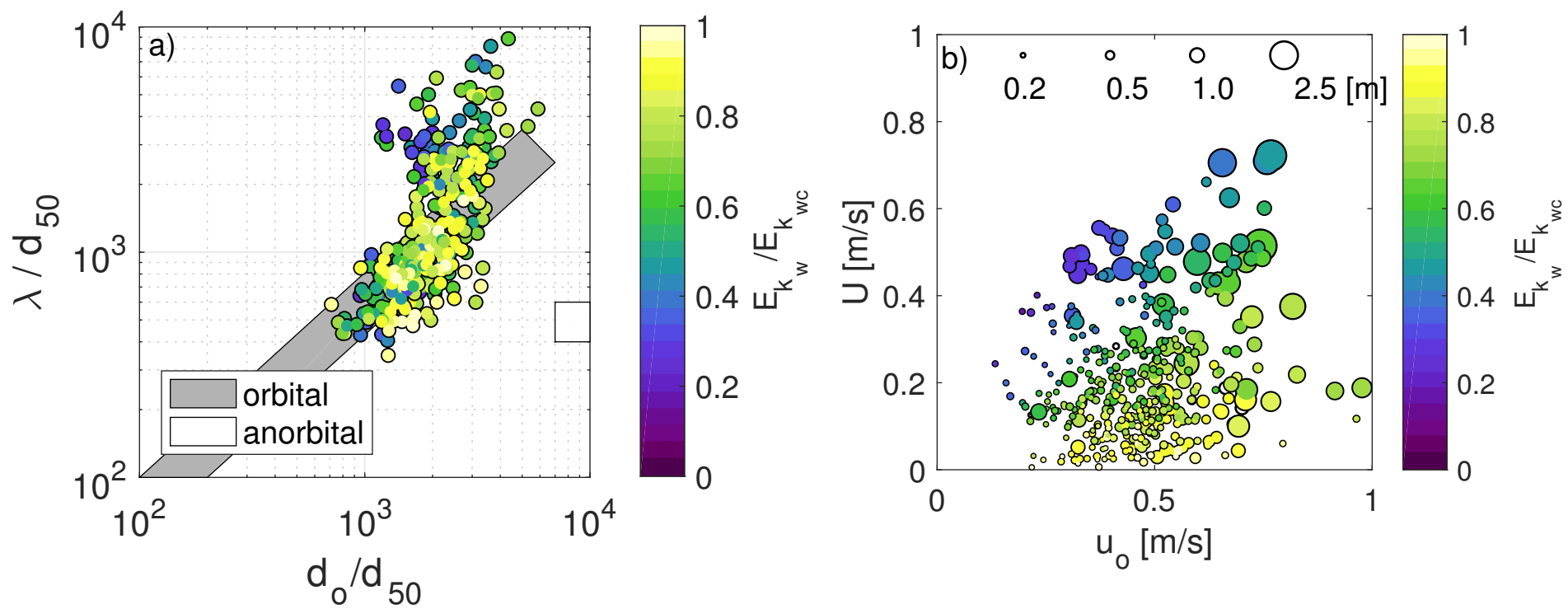


Figure 7.

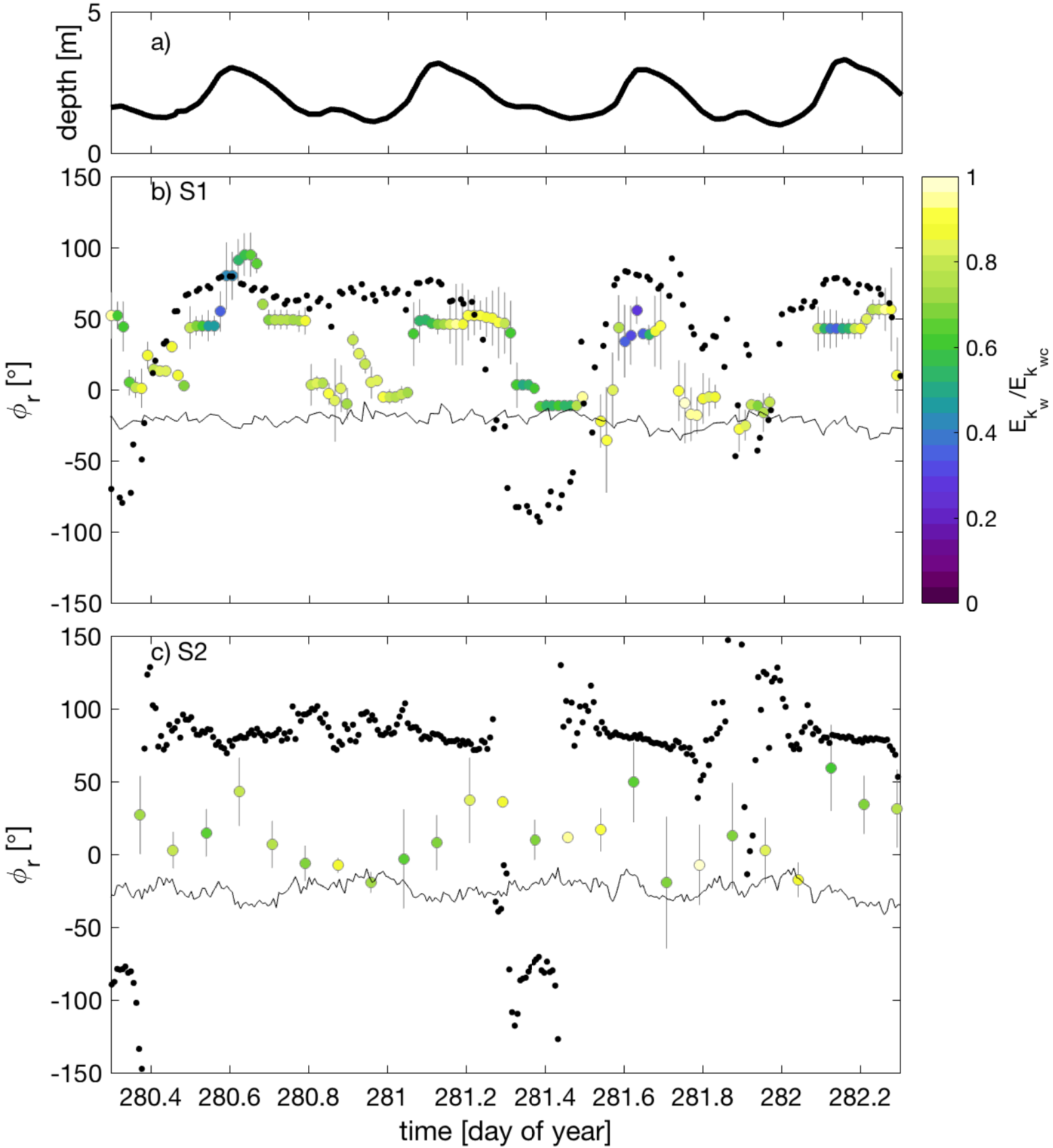


Figure 8.

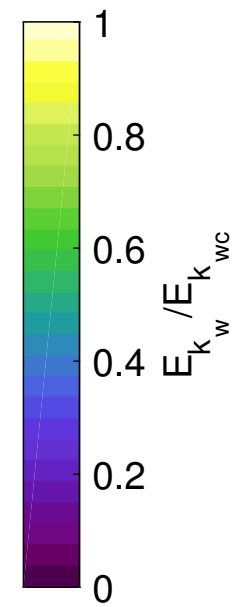
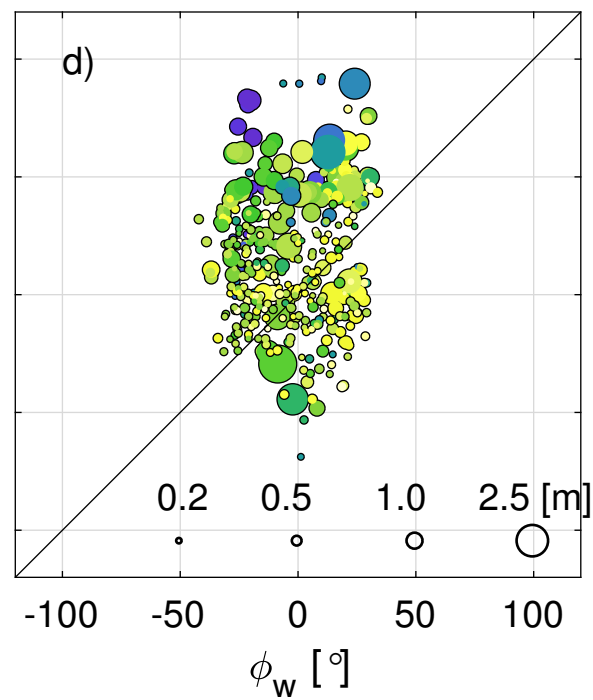
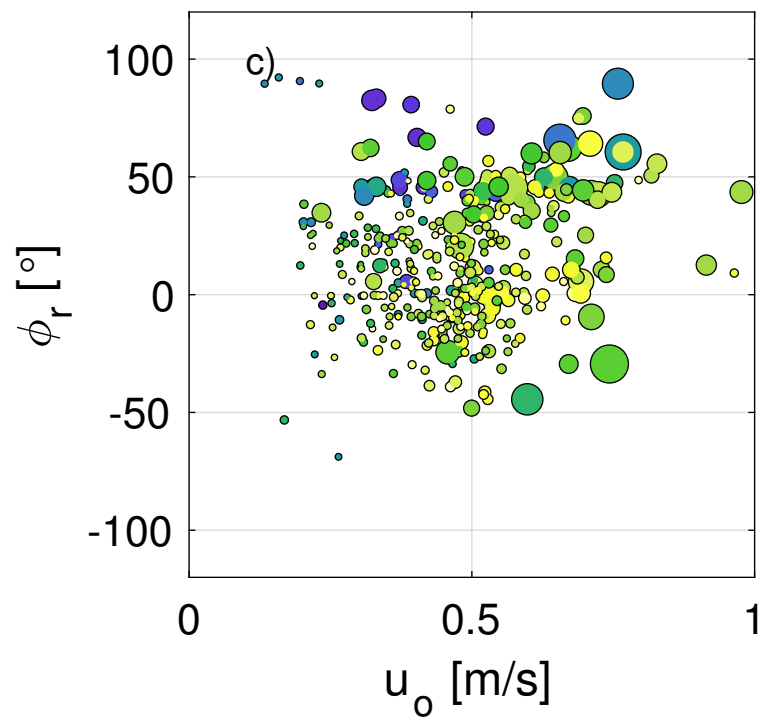
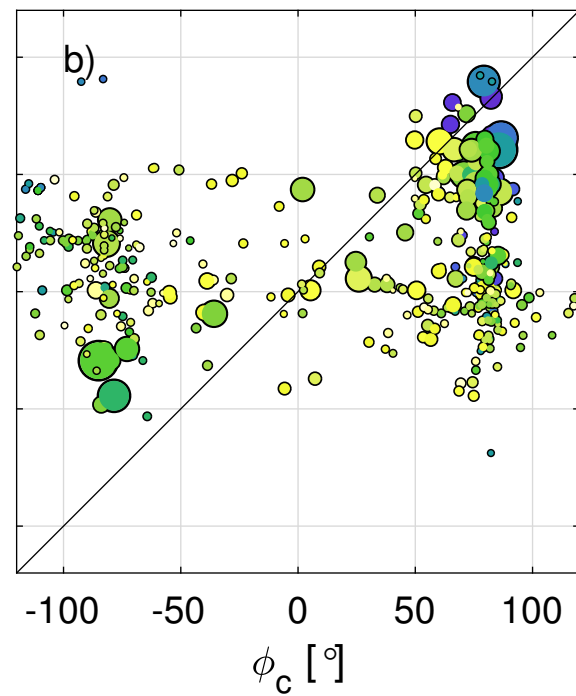
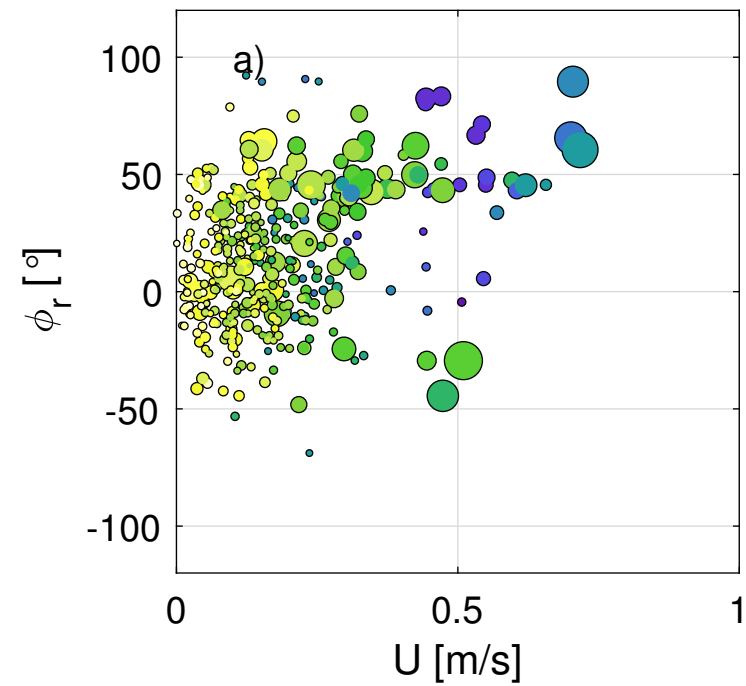


Figure 9.

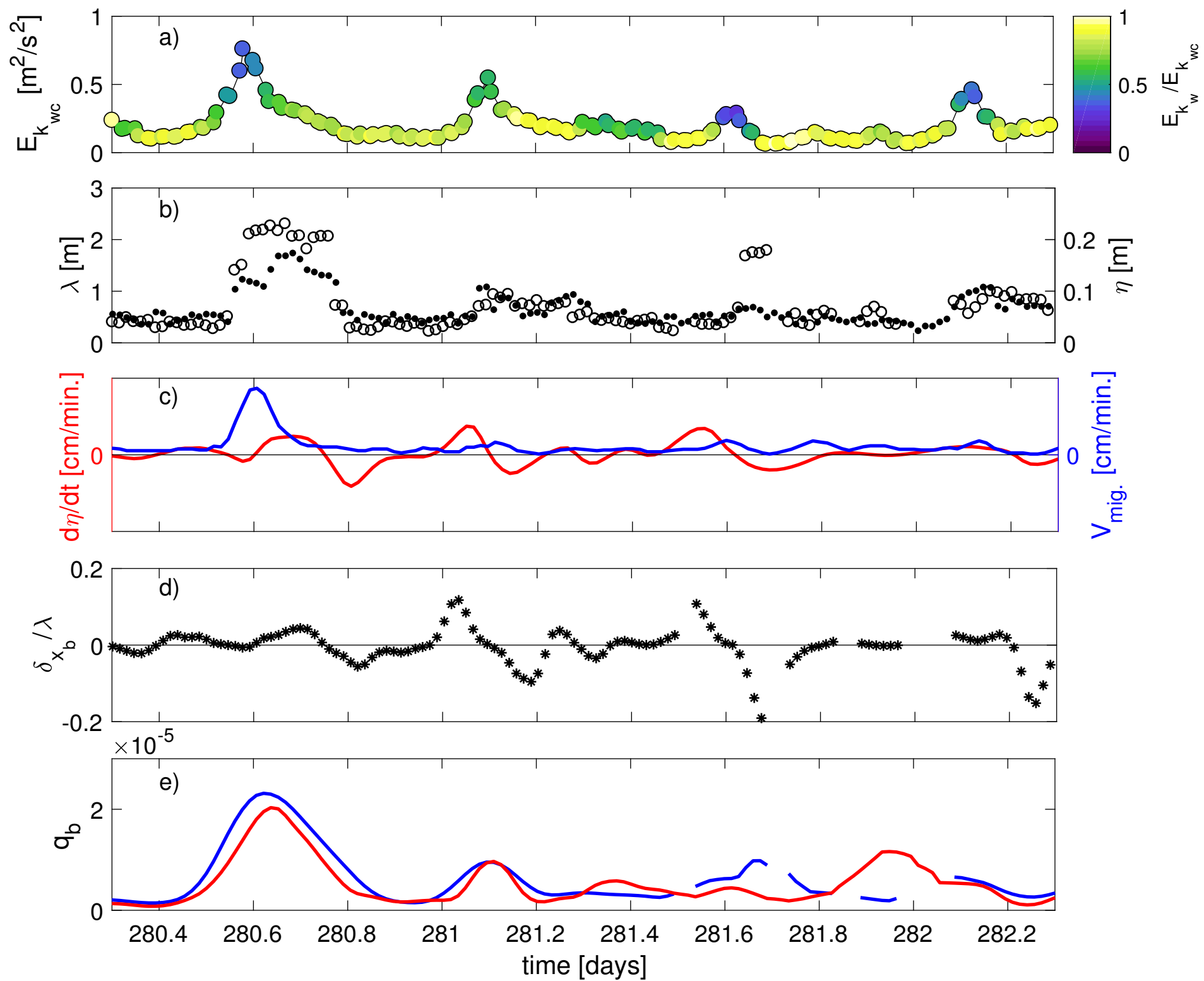


Figure 10.

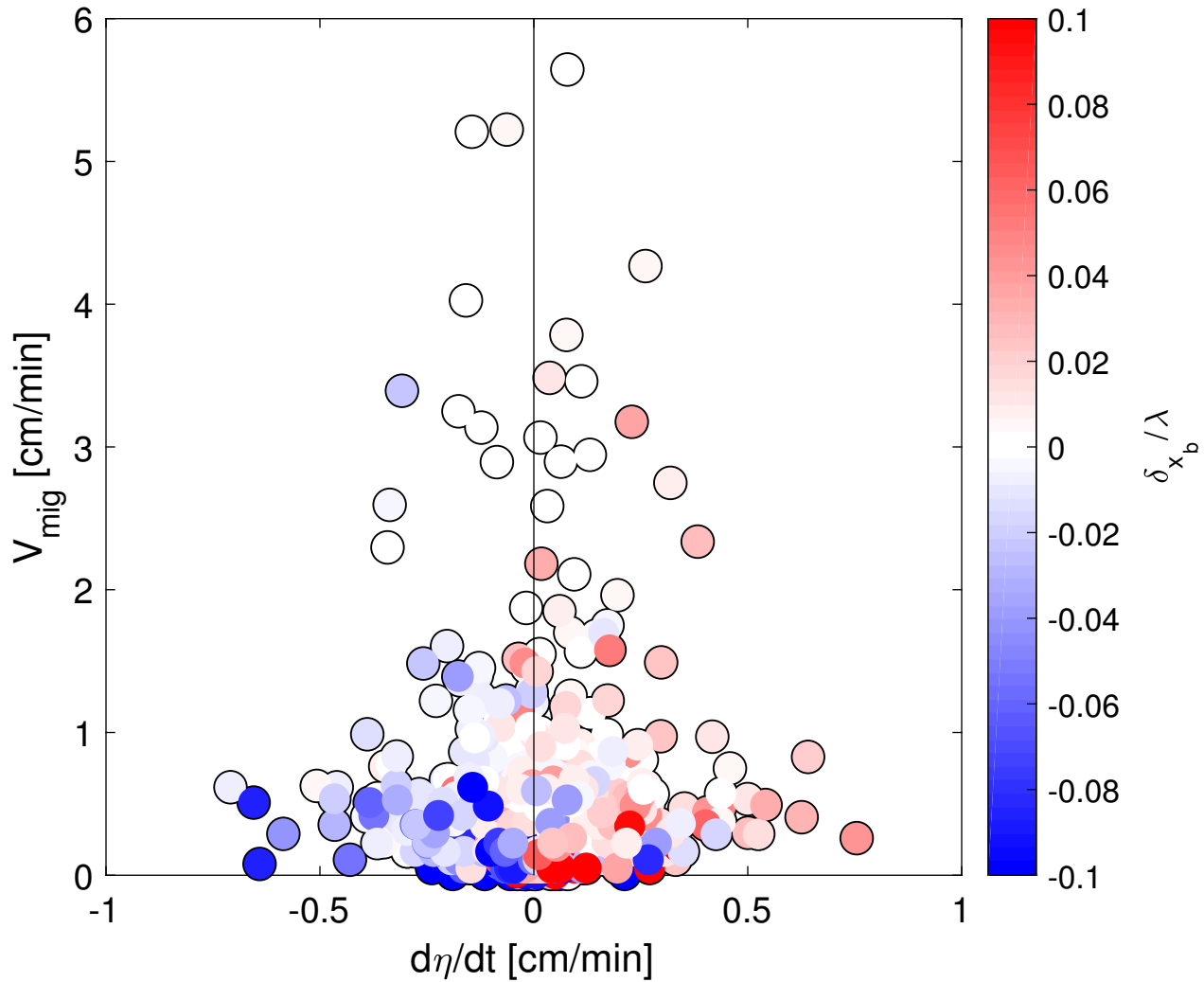


Figure 11.

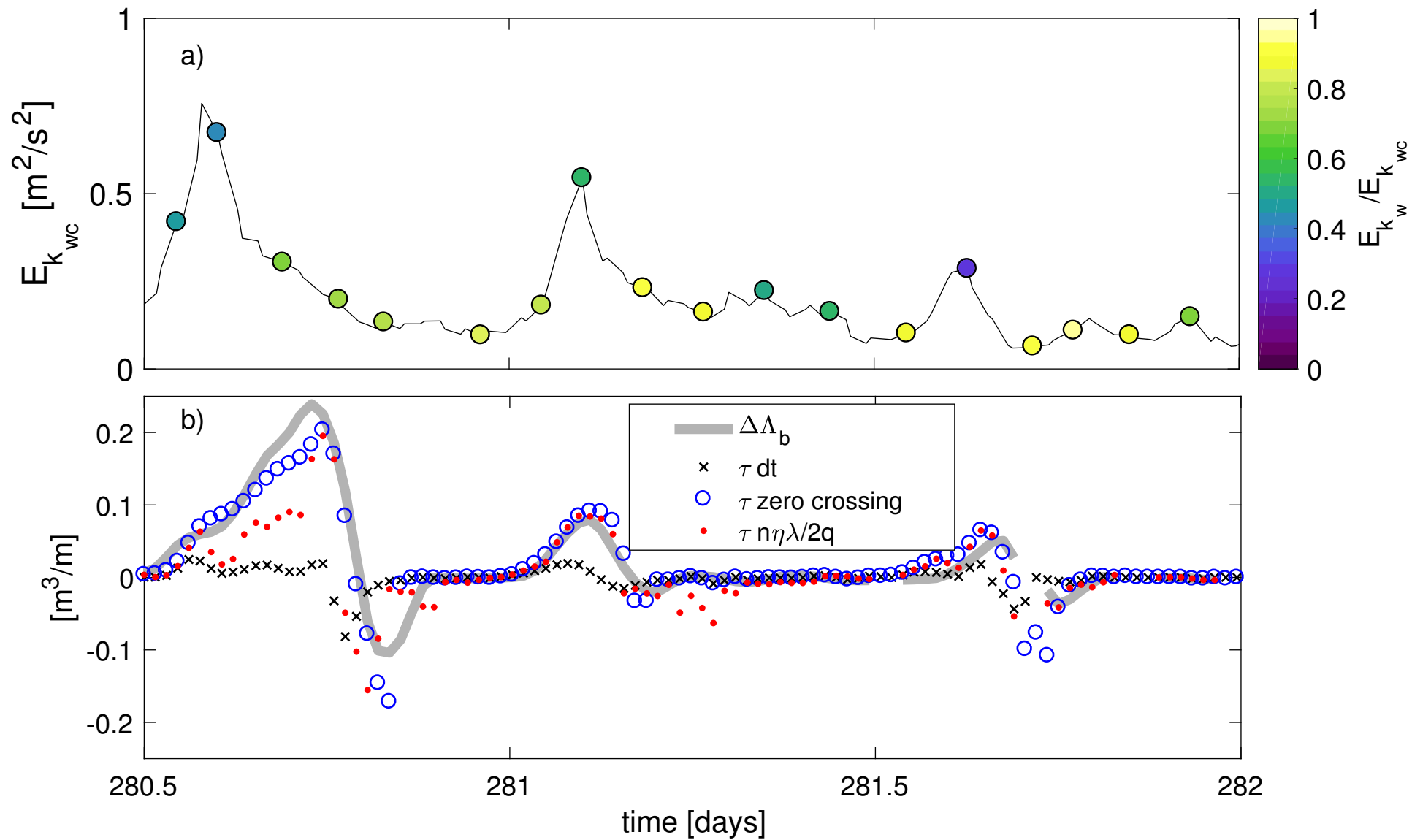


Figure 12.

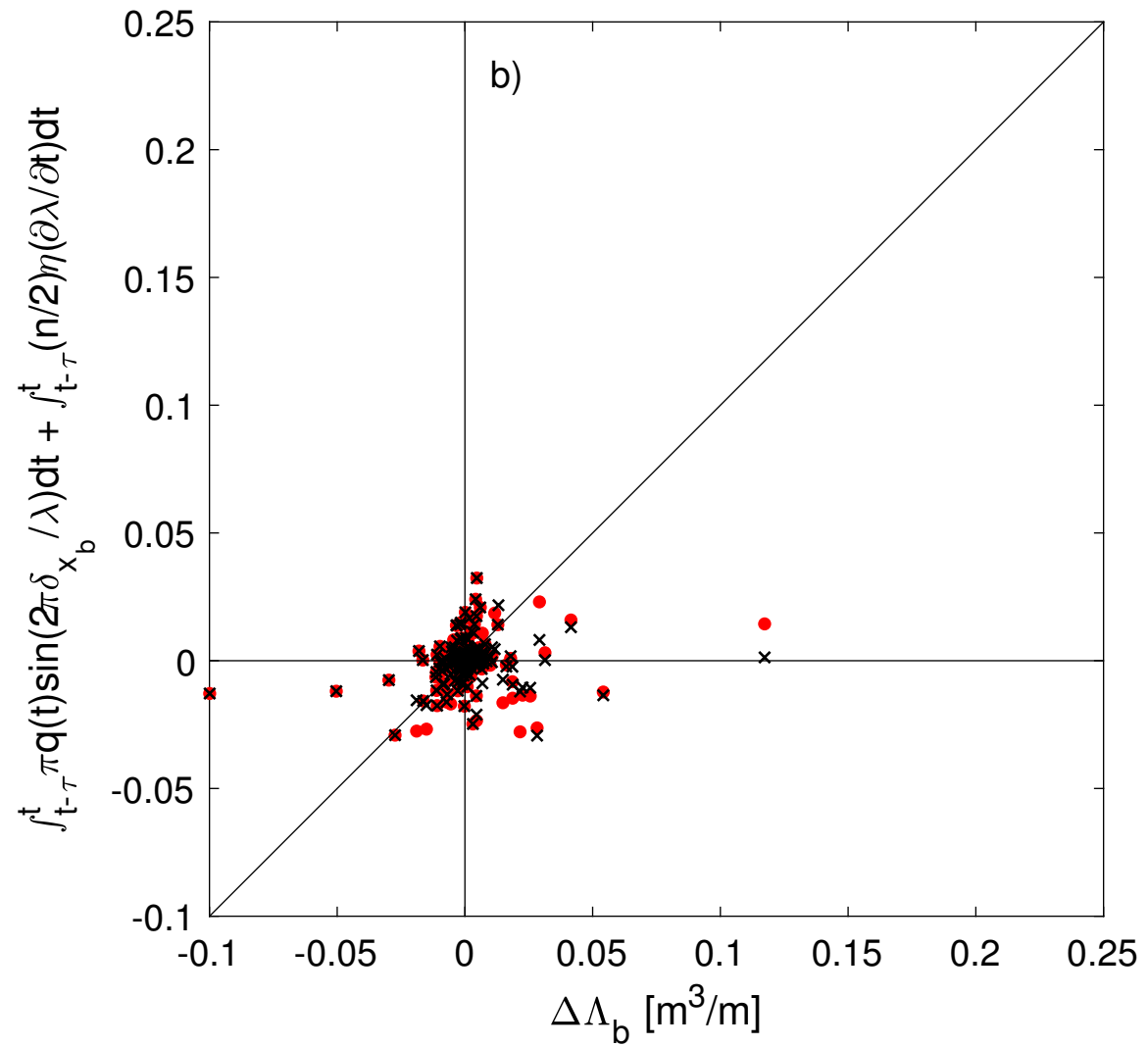
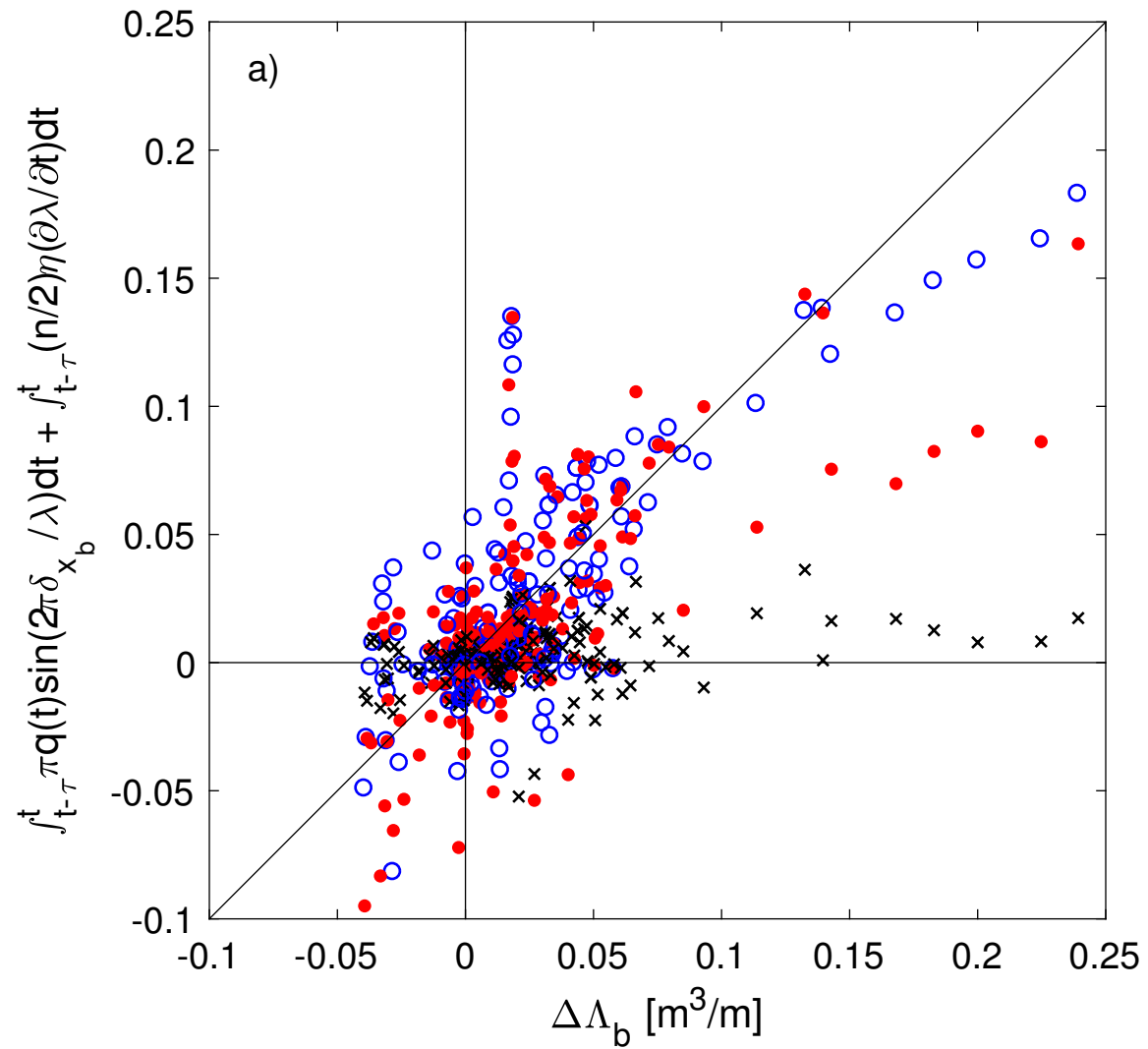


Figure 13.

